A model for the formation of stellar associations and clusters from giant molecular clouds

Michael Y. Grudić[1]⋆, J. M. Diederik Kruijssen[2], Claude-André Faucher-Giguère[1],
Philip F. Hopkins[3], Xiangcheng Ma[4], Eliot Quataert[4], and Michael Boylan-Kolchin[5]

[1]*Department of Physics and Astronomy and CIERA, Northwestern University, 2145 Sheridan Road, Evanston, IL 60208, USA*
[2]*Astronomisches Rechen-Institut, Zentrum für Astronomie der Universität Heidelberg, Mönchhofstraße 12-14, 69120 Heidelberg, Germany*
[3]*TAPIR, Mailcode 350-17, California Institute of Technology, Pasadena, CA 91125, USA*
[4]*Department of Astronomy and Theoretical Astrophysics Center, University of California Berkeley, Berkeley, CA 94720*
[5]*Department of Astronomy, The University of Texas at Austin, 2515 Speedway, Stop C1400, Austin, TX 78712, USA*

ABSTRACT

We present a large suite of MHD simulations of turbulent, star-forming giant molecular clouds (GMCs) with stellar feedback, extending previous work by simulating 10 different random realizations for each point in the parameter space of cloud mass and size. It is found that once the clouds disperse due to stellar feedback, both self-gravitating star clusters and unbound stars generally remain, which arise from the same underlying continuum of substructured stellar density, ie. the hierarchical cluster formation scenario. The fraction of stars that are born within gravitationally-bound star clusters is related to the overall cloud star formation efficiency set by stellar feedback, but has significant scatter due to stochastic variations in the small-scale details of the star-forming gas flow. We use our numerical results to calibrate a model for mapping the bulk properties (mass, size, and metallicity) of self-gravitating GMCs onto the star cluster populations they form, expressed statistically in terms of cloud-level distributions. Synthesizing cluster catalogues from an observed GMC catalogue in M83, we find that this model predicts initial star cluster masses and sizes that are in good agreement with observations, using only standard IMF and stellar evolution models as inputs for feedback. Within our model, the ratio of the strength of gravity to stellar feedback is the key parameter setting the masses of star clusters, and of the various feedback channels direct stellar radiation (photon momentum and photoionization) is the most important on GMC scales.

Key words: galaxies: star formation – galaxies: star clusters: general – stars: formation

1 INTRODUCTION

Star formation (SF) is a statistically-correlated process. It is in some sense *clustered*, with most stars forming as part of stellar structures of elevated stellar density (Lada & Lada 2003; McKee & Ostriker 2007; Krumholz et al. 2019). This clustering in space is accompanied by clustering in time, with the age spread of a population monotonically increasing with the size of the region over which it is measured (Efremov & Elmegreen 1998). In local galaxies, SF is dominated by massive complexes formed in the most massive giant molecular clouds (GMCs), of mass scale $10^6 - 10^7 M_\odot$ in local galaxies (Bolatto et al. 2008; Colombo et al. 2014; Miville-Deschenes et al. 2017; Freeman et al. 2017). Many important questions remain regarding the detailed relationship between giant molecular clouds, young stellar associations, and the

subset of stars formed that are in gravitationally-bound star clusters.

The most basic question is what fraction of the gas mass of of a GMC is converted to stars, the *star formation efficiency* (SFE). Observationally, this can be inferred from measurements of the present gas mass and stellar mass in star-forming regions. Although such estimates of the ratio of young stellar to gas mass have yielded instantaneous SFEs ranging over many orders of magnitude ($\sim 10^{-4} - 1$) (e.g. Myers et al. 1986; Lee et al. 2016; Vutisalchavakul et al. 2016), observations appear to be consistent with a picture where GMCs convert a few per cent of their mass into stars, once the scatter due to molecular cloud evolution is accounted for (see Feldmann & Gnedin 2011, Lee et al. 2016, Grudić et al. 2019, Kruijssen et al. 2019b, Chevance et al. 2020b). This efficiency is largely consistent with theoretical models wherein GMCs are disrupted by feedback from main sequence massive stars (Williams & McKee 1997; Krumholz et al. 2006; Fall et al. 2010; Murray et al. 2010; Kim et al. 2018b; Chevance et al. 2020a). In a previous

⋆ E-mail: mike.grudic@northwestern.edu

study (Grudić et al. 2018a), we presented MHD simulations of star formation in gas clouds with a wide range of parameters including multiple feedback channels, finding that the cloud surface density sets the relative strengths of feedback and gravity, and hence the SFE achieved before the cloud is disrupted. In Grudić et al. (2019), we found that this picture successfully reproduces the measured instantaneous star formation efficiencies of GMCs in the Milky Way in detail (see also Geen et al. 2017).

A complete theory of star formation in GMCs must go further, describing not only how many stars form, but how those stars are organized spatially and dynamically. Regarding this, an important distinction to be made is between *monolithic* and *hierarchical* pictures of star formation. In the monolithic scenario, all stars originate in star clusters of high stellar density, most of which subsequently expand and dissolve into the field due to gas expulsion and N-body evolution (Lada & Lada 1991; Kroupa et al. 2001). In the hierarchical scenario, stellar structure is inherited from a hierarchy of ISM structure spanning a wide range of scales. As a result, stars form with a wide range of natal stellar densities, and gravitationally-bound, dynamically-relaxed clusters are simply the result of the upper tail-end of a larger continuum that happens to have locally-high star formation efficiency (Elmegreen 2002; Elmegreen 2008; Bonnell et al. 2011; Kruijssen 2012). The observational case for the latter scenario has strengthened in recent years, with the general finding that young stellar structure does indeed appear to span a broad range of scales and a continuum of densities (Bastian et al. 2005; Bressert et al. 2010; Gouliermis et al. 2015; Grasha et al. 2017; Gouliermis 2018). Recently it was also found that the kinematics of OB assocations are incompatible with the hypothesis that they consist only of formerly-dense clusters that have since expanded (Ward & Kruijssen 2018; Ward et al. 2020).

The next important question after the SFE is the fraction of the stars locked into bound clusters at the end of star formation:

$$f_{\rm bound} = \frac{M_{\star,\rm bound}}{M_\star}. \tag{1}$$

It has long been thought that the value of $f_{\rm bound}$ is typically $\ll 1$, at least in the conditions of local galaxies (Elmegreen 1983). Simple physical arguments can be made that $f_{\rm bound}$ is an increasing function of the local star formation efficiency (Hills 1980; Mathieu 1983), which have been refined by N-body experiments (Fellhauer & Kroupa 2005; Baumgardt & Kroupa 2007; Smith et al. 2011, 2013). In the monolithic picture, $f_{\rm bound}$ corresponds to the fraction of clusters that survive "infant mortality", the expansion that occurs when gas within the cluster is expelled by stellar feedback. Within the hierarchical picture, it has been argued that bound clusters form in regions where feedback is inefficient, *exhausting* gas locally so that they generally avert infant mortality (Kruijssen et al. 2012; Dale et al. 2015; Ginsburg et al. 2016). Meanwhile, there would be a population of stars that never get a chance to orbit within a bound, virialized structure in the first place – in this scenario, $f_{\rm bound}$ corresponds to the mass fraction of the population that *does* exist within a bound cluster (Bastian 2008; Kruijssen 2012).

It has historically been quite difficult to reliably measure $f_{\rm bound}$ through direct observations of any one star-forming cloud complex, as very good astrometric data are needed[1]. On the other hand, under certain assumptions, it is possible to measure an average $f_{\rm bound}$ integrated over an entire galaxy or a patch of a galaxy (Bastian 2008; Goddard et al. 2010):

$$\Gamma = \frac{\dot{M}_{\rm bound}}{\dot{M}_\star}, \tag{2}$$

where $\dot{M}_{\rm bound}$ and $\dot{M}_\star$ are the mass formation rates of stars in bound clusters and of all stars in the region. Extragalactic studies can only determine the formation rate of stars in dense stellar structures, $\dot{M}_{\rm dense}$, by measuring the mass in dense stellar structures within a certain age bin, and stellar density is not necessarily a sufficient condition for boundedness. However, it is a reasonable approximation if measured over a proper choice of age bin, using only clusters that are too old to have survived as an unbound entity (i.e. older than their internal crossing time, $\sim 1\,{\rm Myr}$), but too young to be likely to be disrupted or to have lost much mass due to galactic or internal dynamical processes ($\leq 100\,{\rm Myr}$) (e.g. Kruijssen & Bastian 2016). This measurement has been performed most convincingly over different regions of several local spiral galaxies (Adamo et al. 2015; Johnson et al. 2016; Messa et al. 2018), with the general finding that regions of greater mean ISM pressure, molecular gas fraction, and gas surface density tend to have greater values of Γ, in line with analytic expectations invoking the progressive inefficiency of stellar feedback toward higher densities (Kruijssen 2012).

Of the material that does remain bound, one must then ask what the properties of the remaining bound structures are. The maximum bound cluster mass in particular is expected to be a sensitive probe of star formation physics, because if GMCs constitute the gas supply potentially available for cluster formation, bound cluster mass satisfies (Kruijssen 2014):

$$M_{\rm cl} \leq f_{\rm bound}\, \epsilon_{\rm int}\, M_{\rm GMC,max}, \tag{3}$$

where $M_{\rm GMC,max}$ is the maximum GMC mass in a given environment, and

$$\epsilon_{\rm int} = \frac{M_\star}{M_{\rm GMC}} \tag{4}$$

is the integrated star formation efficiency of the cloud. Both $f_{\rm bound}$ and $\epsilon_{\rm int}$ are expected to be sensitive to the strength of stellar feedback, so $M_{\rm cl}$ is *doubly* sensitive. Note that Equation 3 does not necessarily hold as an equality because one GMC can potentially produce multiple bound clusters – GMCs can and do produce star cluster *complexes*, where the distribution of cluster masses is described by some underlying distribution.

In this paper we use numerical simulations to approach the above questions about the nature of star cluster formation. We extend our previous work that focused on various aspects of the SFE of GMCs (Grudić et al. 2018a, 2019; Hopkins & Grudić 2019; Grudić & Hopkins 2019), using an expanded suite of numerical simulations to map out the behaviour of star-forming GMCs across parameter space, and, crucially, across 10 different random realizations for the initial turbulent flow of each cloud model. From these numerical results we construct a model that predicts the following statistical properties of star cluster populations formed in GMCs:

- Their star formation efficiency.
- The fraction of stars formed that are locked into gravitationally-bound clusters.
- The mass function of bound star clusters, determined at the level of individual clouds.
- The size-mass relation of bound clusters.
- The initial density profiles of bound clusters.

In doing so, we link the physics of MHD turbulence, gravity, ra-

---

[1] However, recently progress has been made in estimating the boundedness of young star clusters in the Milky Way, see e.g. Ginsburg & Kruijssen (2018) and Kuhn et al. (2019).

diative processes, star formation, and stellar feedback to the observables that provide the most sensitive probes of star formation physics, in a self-consistent framework, and show that this framework contains the necessary and sufficient ingredients to reproduce these key observations.

This paper is structured as follows. In §2, we describe our simulation and analysis methods, and present the raw numerical results of the study. In §4, we describe an analytic statistical model for mapping clouds onto cluster populations that reproduces the results of the simulations, and can be applied to a general cloud population. In §5, we compare model predictions with observations in M83, and demonstrate that the model can recover realistic star cluster properties from observed GMC properties. In §6, we discuss various predictions and applications of our model, and compare it with other models. Finally, in §7, we summarize our main findings and outline future work.

2 SIMULATIONS

2.1 Numerical Methods

We perform a suite of simulations of isolated GMCs with GIZMO, a mesh-free, Lagrangian finite-volume Godunov code designed to capture the advantages of both grid-based and smoothed-particle hydro-dynamics (SPH) methods, described fully in Hopkins (2015) [2]. We solve the equations of ideal magnetohydrodynamics using the Lagrangian Meshless Finite Mass (MFM) method (Hopkins & Raives 2016), augmented with a novel constrained-gradient method to further reduce $\nabla \cdot \mathbf{B}$ errors (Hopkins 2016).

2.1.1 Gravity

The gravitational field is summed using the fast, approximate Barnes & Hut (1986) tree algorithm introduced in GADGET-3 (Springel 2005). However, we have modified the original node-opening criterion used in the GADGET-3 algorithm for our problem. In the original algorithm, a node was opened if the estimated field contribution of its quadrupole moment was greater than some small fraction of the total field at the point of interest. In our problem, this can allow the external tree-force on a dense star cluster to be degraded in accuracy due to its locally-strong gravitational field. To avoid this, we enforced the Barnes & Hut (1986) geometric node-opening criterion with an opening angle $\Theta = 0.5$, in addition to the standard Springel (2005) criterion. The gravitational softening of both gas and star particles is adaptive, with correction terms to ensure energy and momentum conservation as as described in Hopkins (2015). A minimum Plummer-equivalent softening of 10^{-2} pc is enforced only for star particles, however we found that the stellar densities needed for this to have a significant effect are almost never achieved in our parameter space.

2.1.2 Star formation

Our simulations do not attempt to resolve the formation, motion, and feedback of *individual* stars. Rather, as in Grudić et al. (2018a), they simulate the stellar mass distribution as an ensemble of collisionless star particles. In Grudić et al. (2018b) we found that this simulation technique succeeds at producing star clusters of a similar density profile shape to observed young, massive star clusters in local galaxies. The star formation criteria are as described in Grudić et al. (2018a): gas cells may only be converted to stars if they are self-gravitating at the resolution scale (the virial criterion, Hopkins et al. 2013), molecular, and in a converging flow.

We do not impose a threshold density for star formation. In our initial experiments varying the density threshold, we found that it was either irrelevant compared to the virial criterion if set low, or clearly imprinted a characteristic, numerically-imposed 3D density on the star clusters if set high. We thus decided to rely mainly on the virial criterion, which is has more physical motivation. However, we initially found that this alone was not strict enough, because momentary noise in the velocity gradient could potentially allow premature star formation, and convergence of cloud star formation histories with resolution was slow because the low-resolution runs would form stars systematically sooner. We therefore adopted a smoothing procedure for the virial criterion. If $\alpha_{\rm vir} = \frac{E_{\rm kin}}{|E_{\rm grav}|}$ is the local virial parameter, then at each timestep we update dimensionless quantity

$$A\left(t + \Delta t\right) = \frac{\Delta t}{\tau}\frac{1}{1 + \alpha_{\rm vir}\left(t\right)} + \left(1 - \frac{\Delta t}{\tau}\right) A\left(t\right), \qquad (5)$$

ie. $A\left(t\right)$ is the quantity $\frac{1}{1+\alpha_{\rm vir}} \in [0, 1]$ exponentially smoothed with an e-folding time τ. Star formation is allowed when $A\left(t\right) > 1/2$, corresponding to $\alpha_{\rm vir} < 1$. We found that setting $\tau = t_{\rm ff}/8$, i.e. smoothing over a window just 1/8 the local freefall time, is sufficient to de-noise the virial criterion. This was necessary to obtain star cluster mass functions that are robust to numerical resolution (see Appendix A).

2.1.3 Cooling and Stellar Feedback

Our treatment of ISM physics and stellar feedback largely follows the FIRE-2 simulations [3], and all algorithms are presented in detail in Hopkins et al. (2018b). We account for an extensive range of radiative cooling and heating processes, using a standard implicit algorithm, and follow cooling down to a numerically-imposed floor of 10 K.

We include all important nuclear-powered stellar feedback mechanisms from main-sequence massive stars: stellar winds, radiation, and supernova explosions, all of which are dominated by the most massive ($\geq 8\,M_\odot$) stars for young stellar populations. Each star particle is assigned feedback fluxes consistent with a simple stellar population with a well-sampled Kroupa (2001) IMF, with luminosities, mass loadings, and momentum fluxes taken from a STARBURST99 (Leitherer et al. 1999) stellar population model (see Hopkins et al. (2018b) for details).

We caution that the results of GMC simulations with stellar feedback *do* depend somewhat on the specific prescription for distributing feedback fluxes among star particles, even assuming a given IMF (Grudić & Hopkins 2019). However, here we will only target the parameter space of relatively massive ($> 10^6 M_\odot$) GMCs, where cloud lifetimes are long compared to the formation time of massive stars, and the IMF should indeed be well-sampled. As such, we expect that the results of this paper are much less sensitive to the small-scale details of how massive star formation is modeled than the less-massive ($10^5 M_\odot$) cloud simulated in Grudić & Hopkins (2019).

---

[2] A public version of this code is available at `www.tapir.caltech.edu/~phopkins/Site/GIZMO.html`.

[3] `http://fire.northwestern.edu`

Mass, energy, and momentum fluxes from stellar winds and supernova explosions are injected into particles within the hydrodynamic stencil surrounding a star particle according to the fully-conservative scheme described in Hopkins et al. (2018a). The energy-conserving Sedov-Taylor phase of individual supernova blast-waves is resolved explicitly in all simulations, with the most coarsely-resolved runs having a mass resolution of $140\,M_\odot$, and most others much finer, down to $2\,M_\odot$.

We use the LEBRON radiative transfer approximation (for details see Hopkins et al. 2018b), which accounts for absorption of single-scattered photons within the a stencil around a star particle (including ionizing radiation, expanding the search radius until ionizing photons are exhausted). Photons not absorbed within the stencil are propagated through the simulation domain using an optically-thin approximation that uses the gravity solver, with extinction corrections at the source and absorber. The radiation field is computed in far-UV, near-UV, optical/NIR and FIR bins, subject to extinction according to appropriate flux-mean opacities, including dust extinction. We have shown in previous work that this radiative transfer approximation gives cloud SFEs in reasonable agreement (factor of ~ 2) with results from an M1 closure scheme (e.g. Rosdahl & Teyssier 2015, as demonstrated in Hopkins & Grudić 2019; Hopkins et al. 2020), and even better agreement with the results of a state-of-the-art adaptive ray tracing scheme (e.g. Kim et al. 2018b, as shown in Grudić & Hopkins 2019).

2.1.4 Cluster identification

We identify self-gravitating star clusters at the end of the simulations with our own version of the SUBFIND algorithm (Springel et al. 2001). This algorithm organizes the stellar density field into a hierarchy of structures surrounding density peaks, and then at each level of the hierarchy subjects the structures to an iterative unbinding procedure to determine each group's gravitationally-bound subset. Cluster membership is determined according to the *smallest* structures in this hierarchy that can be constructed. We use fast neighbor-lookup and gravitational potential routines provided by scipy (Jones et al. 2001) and pykdgrav[4], respectively. We have also run our analysis using the simpler cluster-finding algorithm described in Grudić et al. (2018b) based on grouping stars into common potential wells, and have found that none of the results of this study were senstive to the choice of algorithm.

2.2 Initial Conditions

Our initial conditions consist of a spherical cloud of uniform density with total mass M_{GMC} and radius R_{GMC}, embedded in a warm, diffuse medium in thermal pressure equilibrium that fills a periodic box of side length $20R_{GMC}$. The initial velocity field of the gas in the cloud consists entirely of a Gaussian random field with power spectrum $|\tilde{v}(\mathbf{k})|^2 \propto k^{-4}$ (Gammie & Ostriker 1996), and a natural mixture of solenoidal and compressive modes (ie. $E_{solenoidal} = 2E_{compressive}$). The velocity field is normalized so that the initial kinetic energy of the cloud is equal in magnitude to its gravitational potential energy. This is a more realistic model of GMCs than the numerical experiments in Grudić et al. (2019), which were intended to isolate a certain surface density scale by ensuring rotational support, which GMCs do not generally have (Braine et al. 2018). The warm, diffuse medium is initially at rest.

[4] https://github.com/mikegrudic/pykdgrav

M_{GMC} ($M_\odot$)	R_{GMC} (pc)	Σ_{GMC} $\left(M_\odot\,pc^{-2}\right)$	α_{turb}	Metallicities ($Z_\odot$)	Realizations
2×10^6	100	63	2	0.01 & 1	10
4×10^6	100	130	2	0.01 & 1	10
8×10^6	100	250	2	0.01 & 1	10
1.6×10^7	100	500	2	0.01 & 1	10
1.8×10^7	300	63	2	0.01 & 1	10
3.6×10^7	300	130	2	0.01 & 1	10
7.2×10^7	300	250	2	0.01 & 1	10
1.4×10^8	300	500	2	0.01 & 1	10

Table 1. Parameter and statistical space of GMC models simulated in this work: initial GMC mass M_{GMC}, radius R_{GMC}, mean surface density $\Sigma_{GMC} = M_{GMC}/\pi R_{GMC}^2$, turbulent virial parameter $\alpha_{turb} = \frac{10E_{turb}R_{GMC}}{3GM_{GMC}^2}$, metallicity, and the number of independent simulations at a given point in parameter space with different random seeds for the initial velocity field.

The magnetic field is initially uniform, and normalized so that the magnetic energy in the cloud is 1% of its turbulent energy.

Our parameter space consists of clouds on a $4 \times 2 \times 2$ grid of surface densities ($64\,M_\odot\,pc^{-2}$, $127\,M_\odot\,pc^{-2}$, $254\,M_\odot\,pc^{-2}$, and $509\,M_\odot\,pc^{-2}$), radii (100 pc and 300 pc), and metallicities (0.01 $Z_\odot$ and $Z_\odot$) (see Table 1). We intentionally targeted a parameter space representative of the largest and most massive GMCs in local spiral galaxies (e.g. Colombo et al. 2014; Rice et al. 2016; Miville-Deschenes et al. 2017; Freeman et al. 2017), for two reasons. We expect that the most massive (and hence most detectable) clusters originate in the most massive GMCs, and that the total mass of stars formed is dominated by the most massive star-forming complexes (e.g. Williams & McKee 1997; Murray 2011; Lee et al. 2016). Hence overall, it is likely that the most massive GMCs produce the dominant contribution to the top end of the observable star cluster mass function, an observation that we will confront in §5. We also expect that this regime of massive star cluster formation is the regime in which our approximations of collisionless stellar dynamics and IMF-averaged feedback are most suitable. Our choice of metallicities is intended to bracket the the range of metallicities of observed globular clusters and galaxies (Usher et al. 2012; Kirby et al. 2013).

In all simulations, the initial cloud component is resolved in 10^6 Lagrangian gas cells of equal mass. For each point in parameter space, we simulate 10 different random realizations of the initial turbulent velocity field. In doing so, we map out not only the *scalings* across parameter space, but the range of intrinsic cloud-to-cloud variations due to small-scale details of the turbulent gas flow, which can potentially be important for star cluster formation.

3 SIMULATION RESULTS

3.1 Global Evolution

All simulations follow the sequence of events that is typical in GMC simulations with a complete accounting of stellar feedback. The initial turbulent motions dissipate on a crossing time-scale (Stone et al. 1998), inevitably leading to localized runaway collapse and eventually star formation. The SFR accelerates at first (Murray & Chang 2015; Lee et al. 2015, 2016), but eventually levels off and begins to drop as feedback begins to evacuate the gas (Feldmann & Gnedin 2011; Grudić et al. 2019; Li et al. 2019). Eventually, all gas is evacuated by feedback and star formation ceases entirely. This process, from start to finish, is illustrated for our fiducial cloud
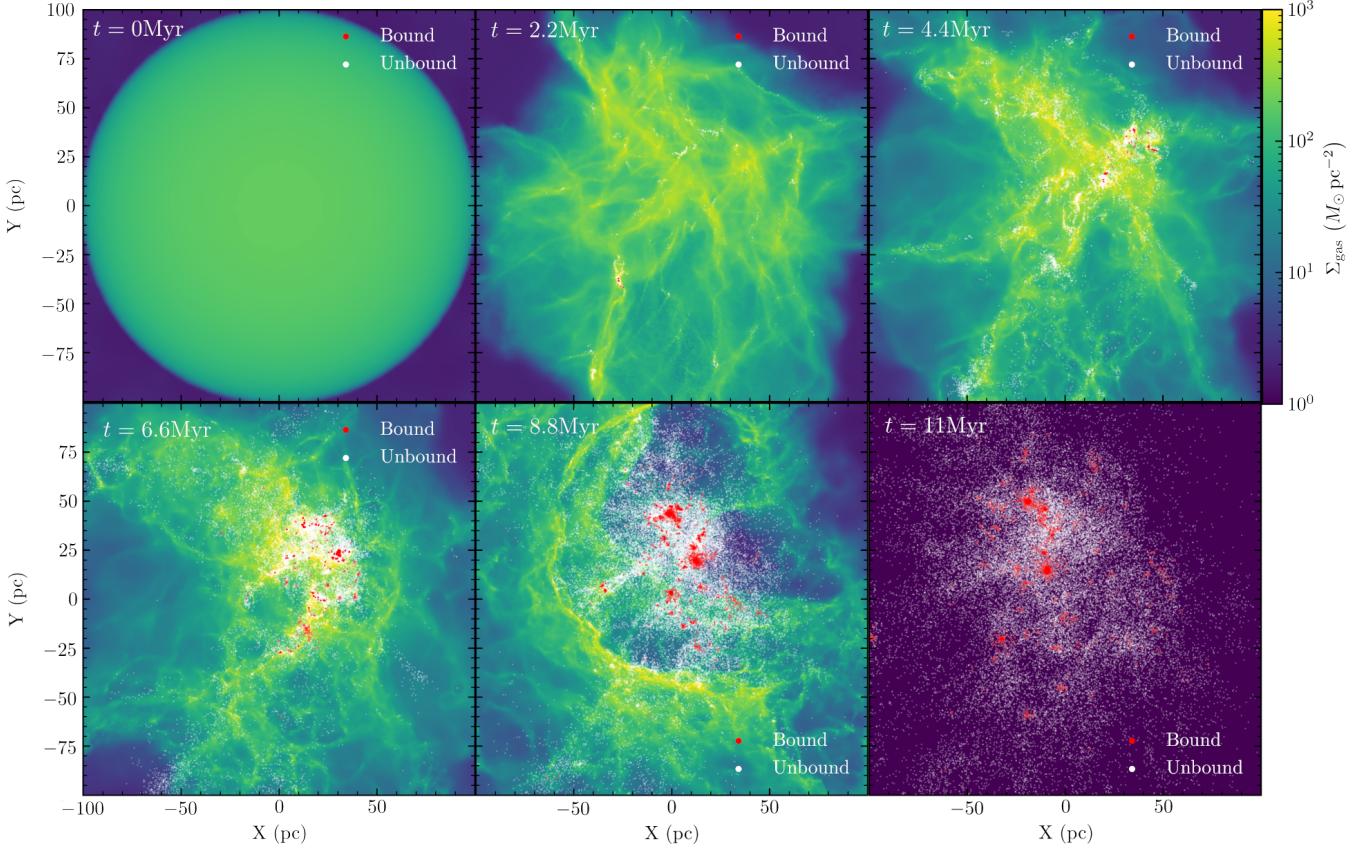
Figure 1. State of the fiducial cloud model with $M = 4 \times 10^6 M_\odot$, $R = 100$pc, and random seed 1 at various points in its evolution (elapsed time given at the top left of each respective panel). Positions of star particles are plotted atop the gas surface density distribution. Star particles not assigned to any bound cluster are shown in white, and bound star particles in red. The GMC produces a highly sub-structured complex of both unbound and bound stellar mass, with most stellar mass in the unbound association in this case ($f_{\mathrm{bound}} \sim 10\%$). This is superfically similar to the configuration of observed complexes of newly-formed stars (see e.g. Kuhn et al. (2014), Fig. 2).

model, with mass $M_{\mathrm{GMC}} = 4 \times 10^6 M_\odot$ and $R_{\mathrm{GMC}} = 100$ pc (Figure 1). All clouds were evolved for two initial cloud free-fall times,

$$t_{\mathrm{ff},0} = \frac{\pi}{2} \sqrt{\frac{R_{\mathrm{GMC}}^3}{G M_{\mathrm{GMC}}}}, \qquad (6)$$

typically on the order of 10Myr for cloud parameters studied here. We generally find that star formation has almost ceased entirely by $\sim 1 t_{\mathrm{ff},0}$, and the central region is essentially gas-free by $2 t_{\mathrm{ff},0}$.

3.2 Star formation efficiency

For this new simulation suite, which has different parameter space and initial cloud kinematics from the Grudić et al. (2019) suite, we repeat the excercise of determining the strongest predictor of the integrated SFE, ϵ_{int}, in terms of the initial cloud parameters. We again find that the cloud surface density Σ_{GMC} is the tightest predictor of ϵ_{int}, in agreement with the picture where ϵ_{int} is primarily determined by the force balance of feedback and gravity within the cloud, which yields a dimensional scaling (Fall et al. 2010; Murray 2011).

We plot the relation between Σ_{GMC} and ϵ_{int} in Figure 2, and see that as before it scales roughly $\propto \Sigma_{\mathrm{GMC}}$, with a modest scatter of 0.1 dex between the different metallicities and statistical realizations of the cloud models, which we will neglect in all subsequent

modeling. We perform an unweighted least-squares fit on $\log \epsilon_{\mathrm{int}}$ as a function of Σ_{GMC} as in Grudić et al. (2019):

$$\epsilon_{\mathrm{int}} = \left(\frac{1}{\epsilon_{\mathrm{int}}^{\max}} + \left(\frac{\Sigma_{\mathrm{GMC}}}{\Sigma_{\mathrm{crit}}} \right)^{-1} \right)^{-1}, \qquad (7)$$

and find best-fit parameters $\Sigma_{\mathrm{crit}} = 3200\,\mathrm{M}_\odot\,\mathrm{pc}^{-2}$ and $\epsilon_{\mathrm{int}}^{\max} = 0.7$[5]. We therefore confirm that the SFE scaling formula of Fall et al. (2010) and Grudić et al. (2018a) still holds for clouds whose internal motions are dominated by turbulence. We also find that our model with $M_{\mathrm{GMC}} = 2 \times 10^6\,\mathrm{M}_\odot$ and $R_{\mathrm{GMC}} = 100$ pc has a SFE of $1 - 3\%$, similar to Grudić et al. (2019) where we used rather different, "pre-stirred" turbulent initial conditions from a driven turbulent box simulation. The details of how turbulence is initialized in isolated cloud simulations does not appear to materially affect the outcome of star formation when feedback is fully accounted for. Of course, both the pre-stirring and Gaussian random field methods are equally artificial, as the initial turbulent motions are not self-consistent with effects of gravity and feedback.

---

[5] We are hardly able to constrain the maximum SFE $\epsilon_{\mathrm{int}}^{\max}$ here due to our choice of parameter space, where the SFE does not exceed 25%, unlike (Grudić et al. 2018a) which surveyed much higher Σ_{GMC} and consequently higher ϵ_{int}.
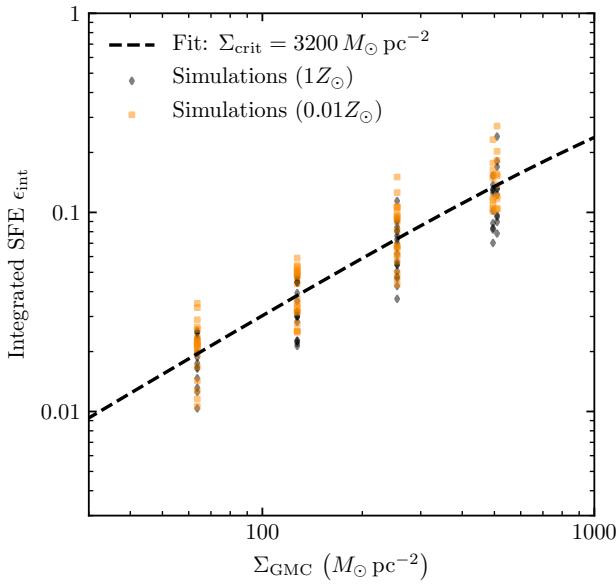
Figure 2. Integrated star formation efficiency $\epsilon_{\mathrm{int}} = \frac{M_\star}{M_{\mathrm{GMC}}}$ as a function of the mean initial cloud surface density, $\Sigma_{\mathrm{GMC}} = \frac{M_{\mathrm{GMC}}}{\pi R_{\mathrm{GMC}}^2}$. ϵ_{int} scales roughly $\propto \Sigma_{\mathrm{GMC}}$, and is well-fit by Equation 7 with $\Sigma_{\mathrm{crit}} = 3200\,\mathrm{M}_\odot\,\mathrm{pc}^{-2}$ and $\epsilon_{\mathrm{int}}^{\mathrm{max}} = 0.68$, with 0.13 dex of residual scatter. This scatter is driven by cloud-to-cloud variations in the details of the initial turbulent gas flow, but is relatively small compared to the scatter in the bound fraction of star formation (e.g. Figure 4).

The relative robustness of the SFE to the different statistical realizations suggests that the star formation efficiency depends simply on the balance of feedback and gravity on the *cloud* scale. Since the cloud bulk properties are essentially a controlled variable here, we accordingly see little variation from cloud to cloud of a given set of parameters.

3.3 The nature of cluster formation

The state of our fiducial cloud model after the end of star formation is plotted in Figure 1 panels 5 and 6, and is qualitatively representative of the result of all simulations in the suite. The result of star formation is a sub-structured, clustered configuration, similar to observed complexes of young stars (e.g. Kuhn et al. 2014; Gouliermis 2018; Ward et al. 2020). Some stars are in bound clusters, but distinct clustered substructures also exist that are not bound. The unbound component eventually disperses in roughly a cloud crossing time, while the respective bound components survive and virialize through violent relaxation.

All simulated clouds produce *some* mass in gravitationally-bound star clusters, although there are a few cases in the lowest-Σ_{GMC} runs where the only cluster masses fall below our resolution cut of 32 particles (which will serve as our resolution cut in this work, as this is roughly the stencil size over which the gravitational softening is adapted). Thus, in the simulations, the formation of bound versus unbound stellar systems are not different modes of star formation, but rather different aspects of the same underlying continuum, consistent with the hierarchical picture of star cluster formation (Kruijssen 2012).

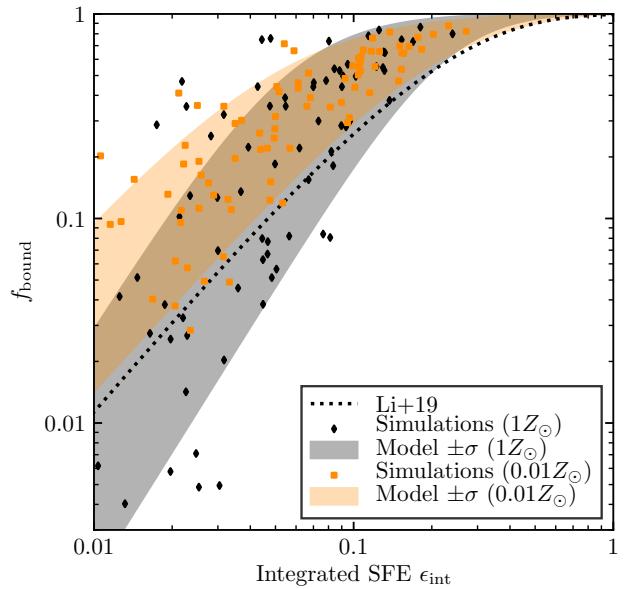This alone does not rule out the monolithic picture: within this

Figure 3. Fraction of stars formed in bound clusters f_{bound} as a function of the integrated star formation efficiency ϵ_{int}. Points are individual simulations, shaded regions are the $\pm\sigma$ contours from the derived statistical model (§4), and the dotted line indicates the fit given by Li et al. (2019) to their simulation results. f_{bound} and ϵ_{int} are correlated, but not generally equal, and with significant scatter from one turbulent realization to another at lower ϵ_{int}. f_{bound} saturates to ~ 1 at a SFE of $\sim 20\%$. It is also systematically greater at low metallicity due to the lack of strong OB winds.

picture, the unbound stellar component at the end of star formation could simply consist of formally-bound clusters that have been disrupted by gas removal. However, we have verified that *final* bound fraction is of the same order (within a factor of ~ 2) as the fraction of stars that have *ever* belonged to *any* structure bound by stellar self-gravity. In other words, the unbound component is dominated by stars that have never had the chance to orbit within a cluster. Therefore, our simulation results are well-described by the hierarchical scenario.

3.4 The bound fraction of star formation

At the end of each simulation, at time $2t_{\mathrm{ff},0}$, we ran the cluster-finding algorithm described in §2.1.4 to group the star particles in to bound star clusters. Across the entire suite, we identified 6181 bound clusters resolved by more than 32 star particles. Every cloud produced at least one bound cluster, and typically multiple ones. As expected from analytic work (Hills 1980; Mathieu 1983), N-body experiments (Tutukov 1978; Lada et al. 1984; Kroupa et al. 2001; Baumgardt & Kroupa 2007), and recent star formation simulations with an idealized feedback model (Li et al. 2019), the fraction of stars remaining in bound clusters at the end of star formation is an increasing function of ϵ_{int} (Fig. 3). Also in agreement with previous numerical works, the bound fraction saturates to ~ 1 at considerably lower SFE than the 50% required in the limit of fast gas evacuation in the classic Hills (1980) derivation – the typical f_{bound} is 50% when $\epsilon_{\mathrm{int}} \sim 10\%$. Systematically higher f_{bound} is achieved at 1% solar metallicity, which we will show in §3.6.1 can be isolated to the lack of strong OB winds, whose mass loss rates scale $\propto Z^{0.7}$ (Vink et al. 2001).
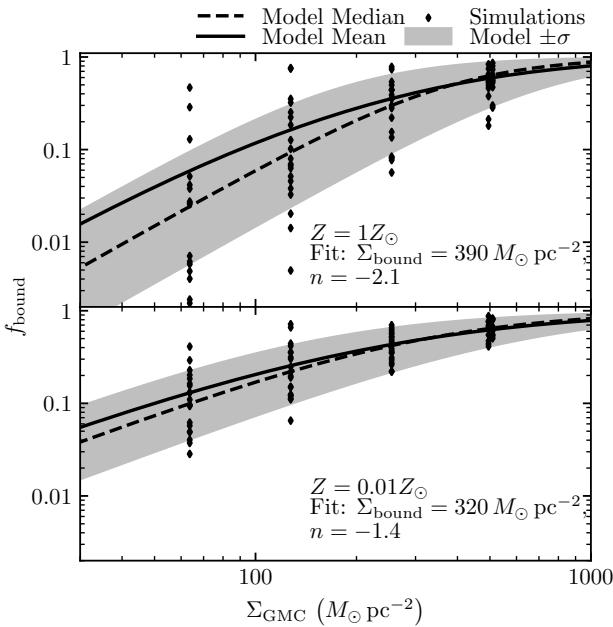
Figure 4. f_{bound}, the fraction of stars in bound clusters at the end of star formation in the simulated GMC, as function of GMC surface density Σ_{GMC} for solar metallicity (*top*) and 1% solar metallicity (*bottom*). We plot the result for each individual simulation (black dots). Unlike the SFE, the relation is notably metallicity-dependent. We perform different fits of equation 8 for each respective metallicity, with best-fit parameters listed above - the solar-metallicity relation is a steeper function of Σ_{GMC}, and reaches the 50% mark at slightly greater surface density. The shaded regions indicate the $\pm\sigma$ region our model for the scatter in f_{bound} (Equations 9 and 10)

.

In Figure 3 we also plot the fit to the semi-analytic model derived in (Li et al. 2019) that summarizes their simulation results. Our results are in reasonably good agreement with this model, modulo a factor of ~ 2 in the SFE where $f_{bound} \rightarrow 1$. This is interesting because their $\Sigma_{GMC} - \epsilon_{int}$ relation was much higher than our Figure 2 for most of their simulations, and yet our simulations lie on nearly the same curve in the $\epsilon_{int} - f_{bound}$ plane. This suggests that this relation is robust to the details of hydro solvers (ie. GIZMO MHD vs. AREPO HD), and feedback model (realistic multi-channel vs. idealized local momentum injection).

The most striking result of Figure 3 is the large scatter in f_{bound} at fixed ϵ_{int}: the relation between the two quantities is not one-to-one, and must be modeled statistically. This is also readily seen in Figure 4, where we plot f_{bound} as a function of Σ_{GMC}. At fixed Σ_{GMC} (which is effectively fixed ϵ_{int} as well), f_{bound} varies by as much as 2 dex, particularly at lower Σ_{GMC}. Surprisingly, there is at least one cloud at any given surface density that is able to form $> 50\%$ of its stars in bound clusters. This result was anticipated by idealized N-body experiments of substructured cluster assembly (Smith et al. 2011, 2013).

Despite the large scatter, a clear scaling in the *typical* bound fraction can be discerned. For each metallicity, we performed unweighted least-squares fits of log f_{bound} to a generic saturating power-law in Σ_{GMC}:

$$f_{bound} = \left(1 + \left(\frac{\Sigma_{bound}(Z)}{\Sigma_{GMC}}\right)^{n(Z)}\right)^{-1}, \tag{8}$$

where $\Sigma_{bound}(Z)$ denotes the metallicity-dependent surface density at which $f_{bound} = 50\%$ and $n(Z)$ is metallicity-dependent power-law slope in the limit $\Sigma_{GMC} << \Sigma_{bound}$. We found $\Sigma_{bound}(Z_\odot) = 390 \, M_\odot \, pc^{-2}$, $\Sigma_{bound}(0.01Z_\odot) = 330 \, M_\odot \, pc^{-2}$, $n(Z_\odot) = -2.1$, and $n(0.01Z_\odot) = -1.4$.

We can model the stochastic variation in f_{bound} shown in Figure 4 by introducing a logarithmic variance in the "effective" value of Σ_{GMC} that is plugged into Equation 8. The effective surface density Σ' is distributed according to a log-normal distribution centered on the actual Σ_{GMC}:

$$P\left(\ln \Sigma' | \sigma_b\right) = \frac{1}{\sqrt{2\pi\sigma_b^2}} \exp\left(\frac{-(\ln \Sigma' - \ln \Sigma_{GMC})^2}{2\sigma_b^2}\right). \tag{9}$$

Once sampled from this distribution, the effective surface density is then plugged into Equation 8:

$$f_{bound} = \left(1 + \left(\frac{\Sigma_{bound}(Z)}{\Sigma'}\right)^{n(Z)}\right)^{-1}. \tag{10}$$

The results of this model are plotted as the shaded regions in Figure 4. We have found that the scatter Σ_{GMC}-dependent scatter in f_{bound} is well-reproduced by the parameter $\sigma_b = 0.7$, ie. the "effective" surface density that matters for star cluster formation varies intrinsically by 0.3 dex from one cloud to another, due to the varying small-scale details of the cluster-forming gas flows.

This procedure can also be repeated to account for the variations in ϵ_{int} (Figure 2, but we find that this is not as nearly important for obtaining a faithful description of the similation results as it is for f_{bound}. First, ϵ_{int} is not as steep a function of Σ_{GMC}, so variations in the "effective" surface density do not compound as drastically. Second, the maximum-likelihood value of σ for modeling variations in ϵ_{int} is less than 1/3 the value required for f_{bound}. We therefore neglect the intrinsic scatter in ϵ_{int} in the results of this work.

3.5 Mass distribution of bound star clusters

As shown in Figure 1, the simulated GMCs typically produce multiple bound star clusters of varying masses and sizes – the mapping from clouds to clusters is not one-to-one. Rather, it must be understood in terms of a *distribution* of cluster masses that emerges at the level of individual clouds. In general, we find that the mass distribution can be described in terms of a primary cluster that dominates (has $\sim 1/10 - 1/2$) of the total mass in bound clusters, and a population of less-massive clusters whose masses are distributed according to a power-law. The mass distribution of bound clusters is robust to numerical resolution (Appendix A).

In Figure 5 we show the stacked cumulative mass functions from all realizations of a give set of cloud parameters – ie., the mass distribution that would be observed if a galaxy formed clusters from many GMCs, but with uniform bulk properties. The distributions are all fairly top-heavy, due to the few particularly massive clusters in the population that constitute the primary cluster in each respective cloud. However, the asymptotic slopes of the mass functions toward lower masses tend to have power-law behaviour, often scaling roughly $\propto M_{cl}^{-1}$, consistent with the mass distribution ~ -2 that is typically measured in young star cluster populations (e.g. Adamo et al. 2020). The mass distributions from the solar metallicity clouds have preferentially shallower slopes, more consistent with a mass function of slope ~ -1.6. It should be noted that the mass distributions in Figure 5 do not in themselves constitute predictions of a galactic star cluster mass distribution, as GMC bulk
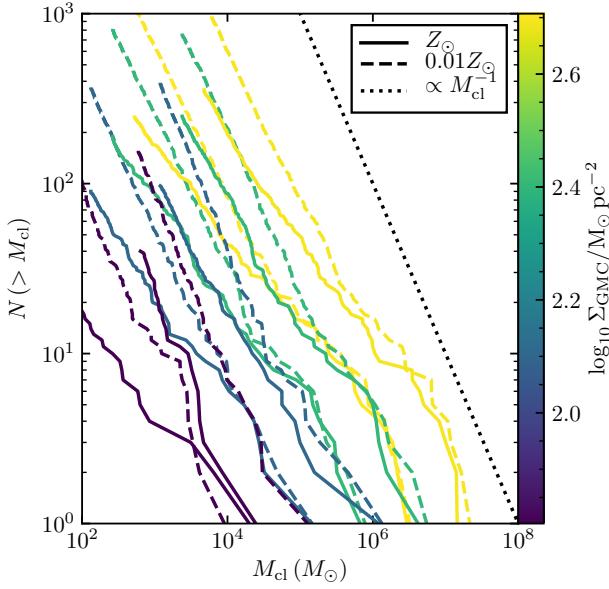
Figure 5. Cumulative mass functions of bound clusters produced by each cloud in parameter space, stacked over the ten random initial turbulent seedings. Curves are colour-coded according to the initial cloud surface density $\Sigma_{\rm GMC}$, and we differentiate between solar-metallicity (solid) and 1% solar metallicity (dashed) cloud models. The dotted line shows the cumulative mass function expected from a typical star cluster mass function of the form $\frac{{\rm d}N_{\rm cl}}{{\rm d}M_{\rm cl}} \propto M_{\rm cl}^{-2}$. See Figure 11 for model predictions of the mass function in a real galaxy.
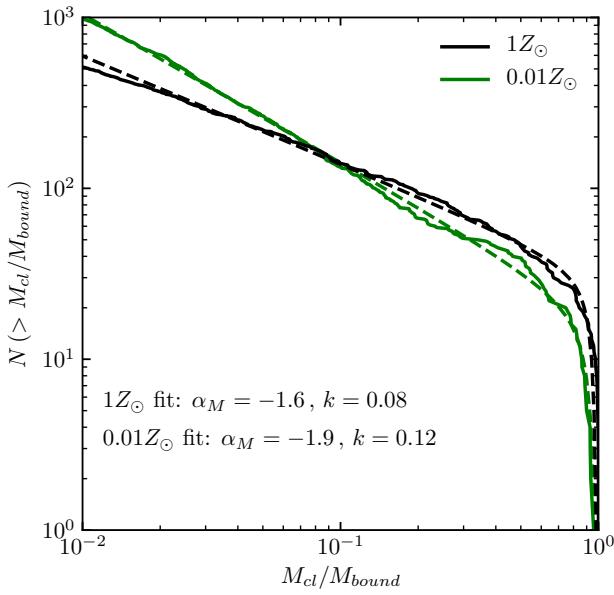
Figure 6. Cumulative distribution of bound star clusters in all simulations, relative to the total bound mass in the respective run. The total mass tends to be dominated by the massive primary cluster. We separate the distributions by metallicity, as the low-metallicity runs tend to have steeper mass functions. Fits to Equation 11 are shown as dashed lines.
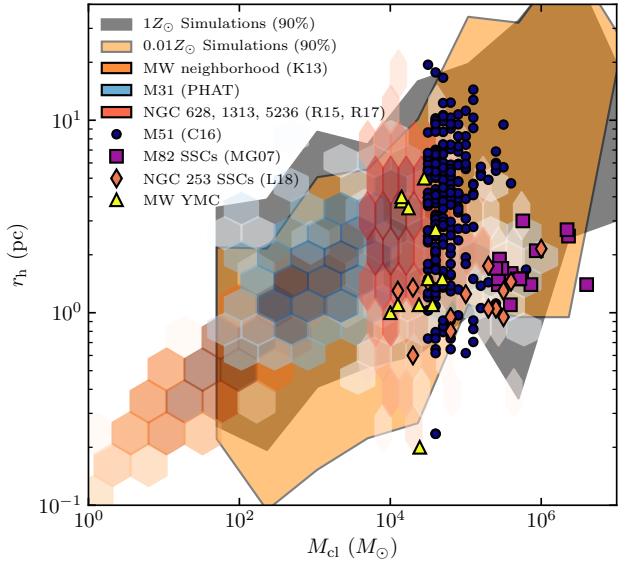
Figure 7. Size-mass relation of the star cluster catalogue extracted from the simulation suite, compared with observed catalogues. We plot the mass-binned contours containing 90% of simulated clusters, with $Z_\odot$ runs and $0.01Z_\odot$ runs shown in grey and green respectively. Observational data include nearby ($< 2\,{\rm kpc}$) clusters in the Milky Way (Kharchenko et al. 2013, K13), Milky Way young massive clusters from the compilation of Krumholz et al. (2019) (MW YMC), and young clusters in NGCs 628, 1313, and 5236 (Ryon et al. 2015, 2017, R15, R17), M31 (Johnson et al. 2012; Fouesneau et al. 2014, PHAT), M82 (McCrady & Graham 2007, MG07), and NGC 254 (Leroy et al. 2018, L18). This figure is largely reproduced from Krumholz et al. (2019) with permission, code and data courtesy of Mark Krumholz.

properties are not uniform in real galaxies. We perform a more-realistic synthesis of observable mass functions in §4.

The cloud-level mass functions can be better summarized when collapsed down in terms of the mass relative to the total bound mass, $M_{\rm cl}/M_{\rm bound}$. In Figure 6 we plot the stacked relative mass functions for the two different metallicities, over all simulations. The cumulative distributions are strongly concave down (such that the PDF $\frac{{\rm d}N_{\rm cl}}{{\rm d}\log M_{\rm cl}}$ is *peaked*) in the vicinity of $M_{\rm cl}/M_{\rm bound}$ because the primary tends to be so dominant, but they then level off to a power-law tail. We fit these cumulative distributions to the model

$$N\left(> M_{\rm cl}\right) = N_0 \left(\frac{M_{\rm cl}}{M_{\rm bound}}\right)^{1-\alpha_{\rm M}(Z)} \exp\left(\frac{-k\left(Z\right)}{1 - \frac{M_{\rm cl}}{M_{\rm bound}}}\right), \quad (11)$$

where N_0 is a normalization factor, $\alpha_{\rm M}\left(Z\right)$ is the slope of the asymptotic power-law mass function for small masses, and $k\left(Z\right)$ is a dimensionless shape parameter that models the heavy top end of the distribution. Again we form metallicity-dependent fits, finding $\alpha_{\rm M}\left(Z_\odot\right) = -1.6$, $k\left(Z_\odot\right) = 0.08$, $\alpha_{\rm M}\left(0.01Z_\odot\right) = -1.9$, and $k\left(0.01Z_\odot\right) = 0.12$. We therefore see that even controlling for GMC properties, a power-law star cluster mass distribution of between -1.6 and -1.9 emerges, due to the cluster multiplicity inherent in hierarchical star formation.

3.6 Size-mass relation

We measured the clusters' projected half-light radii r_h integrated along the z axis in the simulation coordinates, centred on the point of maximum intensity. We caution that unlike cluster masses, our cluster sizes do exhibit some systematic dependence upon numerical resolution (see Appendix A) in the range of mass resolutions we simulated: the clusters were systematically smaller and denser at higher resolution. This may be an unavoidable artifact of our collisionless approximation, as at some point stellar dynamical effects should be important for limiting the phase-space density of stars. Therefore we do not rule out that our results here are subject to numerical effects. Nevertheless, for modeling purposes, we will find that the model derived from our simulations succeeds at reproducing star clsuter sizes *a posteriori* in Section 5, so we still present the basic simulation results here.

The values of r_h we obtained are summarized in Figure 7, where we compare the range of sizes of simulated star clusters with various populations of clusters in the local Universe. We find that the simulated clusters generally do lie in the space of mass and size of observed young star clusters, with less-massive clusters tending to be smaller and vice versa, but with such a weak dependence that no trend at all would likely be seen in a cluster catalogue spanning < 2 dex in mass. As with real star cluster populations, the most salient feature of the simulated mass-size relation is the considerable *dispersion* at fixed mass. Across the entire simulated catalogue, we find a dispersion in cluster size of 0.5 dex, which remains roughly constant with mass.

We have tried fitting r_h to a general power-law of the form $\propto M_{GMC}^{\alpha_1} \Sigma_{GMC}^{\alpha_2} Z^{\alpha_3} M_{cl}^{\alpha_4}$, and the logarithmic least-squares best fit is best predicted by

$$r_h = 3\,\mathrm{pc} \left(\frac{M_{GMC}}{10^6\,M_\odot} \right)^{\frac{1}{5}} \left(\frac{\Sigma_{GMC}}{100\,M_\odot\,\mathrm{pc}^{-2}} \right)^{-1} \left(\frac{Z}{Z_\odot} \right)^{\frac{1}{10}} \left(\frac{M_{cl}}{10^4\,M_\odot} \right)^{\frac{1}{3}}, \tag{12}$$

with ± 0.4 dex of residual scatter that is not driven by variations in the quantities considered above, which is well-approximated by a log-normal distribution. Thus, although the intrinsic scatter is considerable, we do find a mass-size relation that is set by the cloud properties. Neglecting the very weak dependencies upon cloud mass and metallicity (assuming $10^6 M_\odot$ and $Z_\odot$), the size-mass relation lies along lines of constant 3D stellar density, with the 3D density of clusters set by Σ_{GMC}:

$$\rho_{eff} \equiv \frac{3 M_{cl}}{8\pi r_h^3} \approx 44\,M_\odot\,\mathrm{pc}^{-3} \left(\frac{\Sigma_{GMC}}{100\,M_\odot\,\mathrm{pc}^{-2}} \right)^3 \pm 1.1\,\mathrm{dex} \tag{13}$$

Assuming that Σ_{GMC} is an increasing function of the mean galactic Σ_{gas}, such an underlying relation might explain the observed characteristic 3D density of young star clusters in local spiral galaxies (the line $\log \rho = 2$ in Figure 7), where most stars form in clouds with $\sim 50 - 100\,M_\odot\,\mathrm{pc}^{-2}$. It may also explain the relative compactness of star clusters formed in starburst galaxies like M82 for their mass (McCrady & Graham 2007) compared to young clusters in typical spiral galaxies: the central region of M82 has a mean gas surface density of $\Sigma_{gas} \sim 500\,M_\odot\,\mathrm{pc}^{-2}$ (Weiß et al. 2001), ie. ~ 5 times greater than the typical GMC surface density in galaxies where clusters lie along the typical size-mass relation, and hence the typical star cluster density is $5^3 \sim 2$ dex greater. However this remains fairly speculative, as a proper numerical comparison would

Run	ϵ_{int}	f_{bound}	$M_{cl,max}$ $(M_\odot)$
Standard, $Z_\odot$	4.6%	6.7%	5×10^3
Standard, $0.01 Z_\odot$	4.3%	22%	10^4
No winds	4.6%	18%	1.3×10^4
No radiation	10.4%	70.4%	2.7×10^5
No SNe	4.6%	5.3%	6×10^3
No feedback	30% +	90%+	$3.2 \times 10^5+$

Table 2. ϵ_{int}, f_{bound}, and the maximum bound cluster mass in test runs that turn off various subsets of the feedback physics included in the standard suite, run for the fiducial cloud with $M_{GMC} = 4 \times 10^6\,M_\odot$ and $R_{GMC} = 100\,\mathrm{pc}$ (for a single turbulence realization). Results of the 'No feedback' model are given with a '+' because this model was only run for half as long as the others, and at this time these quantities were still rising.

require Σ_{GMC} to be known, and likely also some accounting for cluster size evolution (e.g. Choksi & Kruijssen 2019).

3.6.1 The roles of different feedback mechanisms

To determine which specific feedback mechanisms are responsible for the setting the various quantities presented in this section, we ran a series of simulations on our fiducial cloud model ($M_{GMC} = 4 \times 10^6\,M_\odot$, $R_{GMC} = 100\,\mathrm{pc}$, and $Z = Z_\odot$) in which we varied the feedback physics included for a single turbulence realization. Specifically, we tried switching off stellar winds, radiation, supernovae, and all feedback mechanisms in turn. We summarize the results of this experiment in Table 2.

Neglecting feedback altogether results in runaway collapse and very high ϵ_{int}, f_{bound}, and star cluster mass. We did not run the no-feedback run past $t_{ff,0}$ due to the computational expense of integrating the extremely dense star clusters that formed, and at this time 30% of the cloud mass had been converted into stars, with no sign of stopping.

Neglecting radiation increased ϵ_{int} from 5% to 10%, and f_{bound} from 7% to 70%. Radiative feedback is therefore apparently crucial in moderating star cluster formation, and also plays the dominant role in setting the cloud-scale SFE, although stellar winds and SNe are still able to moderate star formation somewhat.

The results of the run neglecting SNe are nearly identical to the standard run, so we find that SNe are practically irrelevant to both the cloud-scale SFE and the formation of bound clusters in this region of parameter space. They are unable to moderate star formation on the scale of cluster-forming clumps because the clusters generally form over much shorter time-scales than the ~ 3 Myr that it takes for the first SNe to go off.

Neglecting stellar winds did not change ϵ_{int} at all. However, the bound fraction and maximum cluster mass of the model with no stellar winds at *solar* metallicity were very close to those of the standard $0.01 Z_\odot$ run. We are therefore able to isolate the metallicity dependence of f_{bound} shown in §3.4 to the effective absence of stellar winds at low metallicity, as this is the only large metallicity dependence of feedback that we model. It is remarkable that stellar winds should affect cluster formation so drastically while leaving the cloud-scale SFE unaltered. In the dense ($\Sigma_{gas} > 10^3\,M_\odot\,\mathrm{pc}^{-2}$) clumps where individual clusters form, it is expected that both radiative feedback and the momentum-injecting component of stellar wind feedback are inefficient (Fall et al. 2010). By contrast, a hot stellar wind bubble that has not had a chance to vent may

behave more in the regime of energy-conserving feedback, which is more efficient than momentum-conserving feedback on small scales: $\epsilon_{\rm int} \propto \Sigma^{\frac{3}{2}} R^{\frac{1}{2}}$, versus being $\propto \Sigma$ for momentum-conserving feedback (Fall et al. 2010).

To summarize, having some type of stellar feedback is crucial for setting both the cloud-scale SFE and the bound fraction of star formation. Radiative feedback is the most important, but stellar winds can be a uniquely efficient feedback mechanism on small scales, potentially affecting the outcome of individual star cluster formation while having modest effects upon the cloud-scale SFE.

4 STATISTICAL MODEL: MAPPING CLOUDS TO CLUSTERS

4.1 Harmonizing cloud parameters

Equipped with general results for $\epsilon_{\rm int}$, $f_{\rm bound}$, and the star cluster size and mass distributions from the previous section, we are nearly ready to construct a statistical model that is able to reproduce our simulation results for any set of GMC parameters. But first, if the model is to be used on observational data, or clouds in a simulated galaxy, we must address some ambiguities in the model inputs: the cloud bulk parameters. For the purposes of the present work we will set aside the observational uncertainties about the interpretation of CO emission as a mass tracer, and assume that the CO to H_2 conversion factor $X_{\rm CO}$ is known.

For real clouds, there is some ambiguity about what the proper cloud size $R_{\rm GMC}$, and more crucially surface density $\Sigma_{\rm GMC}$ to use is, as real clouds are not uniform spheres. For a general mass distribution $\rho(\mathbf{x})$, we will define $R_{\rm GMC}$ as the radius of a sphere of equal moment of inertia:

$$R_{\rm GMC} \equiv \sqrt{\frac{5}{3M_{\rm GMC}} \int \rho(x) r^2 \, \mathrm{d}^3\mathbf{x}}, \qquad (14)$$

where r is the distance from the cloud centre of mass. This trivially reduces to our definition for a spherical top-hat distribution.

A common definition of the effective radius used in GMC catalogues is the root mean square of the intensity-weighted second moments of the 2D CO intensity (e.g. Freeman et al. 2017). For a Gaussian cloud model, assuming CO intensity maps directly onto surface density, this definition is a factor of $\sqrt{3}$ less than the definition in Equation 14, and is a factor of $\sqrt{\frac{15}{2\pi}}$ less for a uniform sphere model. The two conversion factors are nearly equal – we will adopt the latter in §5.

Another common definition of the effective radius of a cloud is the radius of a circle with area equal to the pixels that the cloud occupies. This is more problematic for us, because it ultimately depends on the specific intensity cut that is used to define the cloud boundary. For this reason, we advise caution if applying this model to data that uses this definition – it is not obvious that the effective radius provided is actually characteristic of the mass distribution of the cloud. A decently representative value of $\Sigma_{\rm GMC}$ is crucial for the model, because this affects both $\epsilon_{\rm int}$ and $f_{\rm bound}$, so cluster masses are doubly sensitive to it. Thus modest errors in $R_{\rm GMC}$ can compound into major errors in star cluster properties.

4.2 Algorithm

Having resolved the ambiguity in cloud size, we are now equipped with the cloud bulk parameters that are the inputs to the model: its

Parameter	Used in	Affects	$Z_\odot$ value	$0.01Z_\odot$ value
$\Sigma_{\rm crit}$	Eq. 7	SFE	$3200\,{\rm M_\odot\,pc^{-2}}$	$3200\,{\rm M_\odot\,pc^{-2}}$
$\epsilon_{\rm int}^{\rm max}$	Eq. 7	SFE	0.8	0.8
$\Sigma_{\rm bound}$	Eq. 10	$f_{\rm bound}$	$390\,{\rm M_\odot\,pc^{-2}}$	$330\,{\rm M_\odot\,pc^{-2}}$
n	Eq. 10	$f_{\rm bound}$	2	1.4
σ_b	Eq 9	$f_{\rm bound}$	0.7	0.7
α_M	Eq 11	Mass function	-1.6	-1.9
k	Eq 11	Mass function	0.08	0.13

Table 3. Summary of model parameters for mapping GMCs onto star cluster populations. None of these are free parameters: the are calibrated to reproduce the star cluster statistics of the simulation results in Section 3.1.

mass $M_{\rm GMC}$, radius $R_{\rm GMC}$, mean surface density $\Sigma_{\rm GMC} = \frac{M_{\rm GMC}}{\pi R_{\rm GMC}^2}$, and metallicity Z. The mapping from clouds to clusters then proceeds as follows:

(i) Compute the metallicity-dependent model parameters provided by the simulations: $\Sigma_{\rm bound}(Z)$, $n(Z)$ (Equation 10), $\alpha_{\rm M}(Z)$, and $k(Z)$ (Equation 11). For an arbitrary metallicity, we use a linear interpolant in $\log Z$, using the values provided at $0.01Z_\odot$ and $Z_\odot$ in Table 3. For any parameter $p(Z)$:

$$p(Z) = \frac{\log_{10}(Z/Z_\odot) + 2}{2} p(Z_\odot) - \frac{\log_{10}(Z/Z_\odot)}{2} p(0.01Z_\odot) \quad (15)$$

(ii) Compute the SFE (Equation 7) and the total stellar mass formed:

$$M_\star = \epsilon_{\rm int} M_{\rm GMC} \qquad (16)$$

(iii) Of this total stellar mass that forms, compute the fraction $f_{\rm bound}$ of this stellar mass in bound clusters with Equations 9 and 10. The total mass in bound clusters is then:

$$M_{\rm bound} = M_{\rm GMC} \epsilon_{\rm int} f_{\rm bound}. \qquad (17)$$

The mass that is not in bound clusters constitutes the unbound association component of the stellar population formed in the cloud.

(iv) Sample the relative cluster masses $M_{\rm cl}/M_{\rm bound}$ from the cloud-level mass distribution (Equation 11), until the sum of the masses exceeds $M_{\rm bound}$. Reject the final cluster if it commits a lesser mass conservation error than keeping it.

(v) Sample the cluster half-mass radii according to a log-normal size distribution with median given by Eq. 12 and with variance 0.4dex.

Finally, using the results of Grudić et al. (2018b), we can also model the specific shapes of the star cluster density profiles. Young star clusters are generally well-fit by the Elson et al. (1987) density profile:

$$\rho(r) = \rho_0 \left(1 + \frac{r^2}{a^2}\right)^{-\frac{\gamma+1}{2}}, \qquad (18)$$

where a is a scale radius, related to the effective radius by

$$a = \frac{r_{\rm h}}{\sqrt{2^{\frac{2}{\gamma-2}} - 1}} \qquad (19)$$

and γ is the power-law slope of the outer surface density profile of the cluster. We found in Grudić et al. (2018b) that γ has a universal distribution in observed and simulation star cluster populations,

that is seemingly uncorrelated with any other cluster property, but is apparently set during the star formation process. For our synthetic cluster population, we sample γ randomly using the following fit to the universal CDF on the interval $\gamma \in [2, 10]$:

$$N(<\gamma) = 1.064 \left(\frac{\gamma - 2}{\gamma - 0.8} \right)^{0.54}. \qquad (20)$$

4.3 Monte Carlo experiments

To build some intuition for the predictions of the model for typical galactic conditions, we now consider its predictions for the star cluster population arising in a simple one-zone galactic ISM model described by the following properties, with respective fiducial values:

(i) Star formation rate: SFR (fiducial value $1 M_\odot \, \mathrm{yr}^{-1}$).

(ii) Distribution of GMC formation rates in GMC mass: $\frac{dN_{\mathrm{GMC}}}{dt \, dM_{\mathrm{GMC}}}$. For our fiducial model, we take a power-law distribution $\frac{dN_{\mathrm{GMC}}}{dt \, dM_{\mathrm{GMC}}} \propto M_{\mathrm{GMC}}^{-2}$ with lower limit $M_{\mathrm{GMC,min}} = 10^3 M_\odot$ and upper limit $M_{\mathrm{GMC,max}} = 10^7 M_\odot$.

(iii) Distribution of GMC surface densities, which we model as a log-normal distribution with mean $\langle \Sigma_{\mathrm{GMC}} \rangle = 50 \, \mathrm{M_\odot \, pc^{-2}}$ and dispersion $\sigma_{\log \Sigma_{\mathrm{GMC}}} = 0.3$ dex, similar to what is found in GMC catalogues in our and nearby galaxies (Miville-Deschenes et al. 2017; Freeman et al. 2017; Faesi et al. 2018; Sun et al. 2018), and in agreement with galactic-scale simulations with stellar feedback and resolved ISM structure (Hopkins et al. 2012; Guszejnov et al. 2020b).

We synthesize star cluster populations from our model by sampling a sufficiently large sample of N_{GMC} GMC masses and surface densities from the formation-rate mass function and Σ_{GMC} distributions respectively, determining the total stellar mass $M_\star$ formed by plugging these into Equation 7, and implicitly determining the times between individual GMC star formation episodes as $\Delta t = M_\star/(\mathrm{SFR} \, N_{\mathrm{GMC}})$. We assume a constant spacing in time Δt, but very similar results were obtained from a random Poisson process with mean GMC formation time-scale equal to this Δt.

In Figure 8 we plot simple mock observations of the mass CDFs for GMCs, stellar associations, and bound star clusters in our model galaxy (taking stellar associations to be the *entire* stellar content formed by a GMC, bound or unbound). We show cumulative GMC and stellar association populations formed in 10 Myr windows (effectively assuming a 10 Myr lifetime, Kruijssen et al. 2019b; Chevance et al. 2020b), and clusters in the age range $10 - 100$ Myr windows for bound clusters, similar to the age bins typically assumed to consist mainly of bound clusters in observations (e.g. Adamo et al. 2015; Johnson et al. 2016; Messa et al. 2018).

Panel a) shows the relationship between the mock-observed mass functions of GMCs, associations, and bound clusters for our fiducial model. The stellar association mass function is essentially the GMC mass function shifted downward by a factor of the SFE, and convolved with a log-normal due to the variance in Σ_{GMC} and hence ϵ_{int}. The mass function of bound clusters is somewhat steeper than that of GMCs or associations, and has less resemblance in shape, with a less-obvious upper truncation at our fiducial SFR. The maximum cluster mass is less than the maximum association mass, but only by a factor of ~ 2, considerably greater than would be assumed by multiplying the maximum stellar association mass by the mean galactic f_{bound} of $\sim 10\%$.

In Figure 8 panel b) we vary the assumed GMC mass distribution, comparing our fiducial truncated power-law with a Schechter (1976)-like $\frac{dN_{\mathrm{cl}}}{dM_{\mathrm{cl}}} \propto M_{\mathrm{cl}}^{-2} \exp(-M_{\mathrm{cl}}/M^*)$ form and a Dirac δ-function, all normalized to have equal mass-weighted median GMC mass. The truncated power-law and Schechter-like models are difficult to distinguish for all 3 mass functions, illustrating the importance of statistical rigor when attempting to distinguish between these models in observations (e.g. Johnson et al. 2017; Mok et al. 2019; Adamo et al. 2020). The δ-function gives the "impulse response" of our model, from which any mass function can be constructed via synthesis. The resulting stellar association mass function is log-normal due to the log-normal Σ_{GMC} and ϵ_{int} distributions, while the bound cluster mass function exhibits a low-mass power-law tail imprinted by the GMC-level mass function.

In Figure 8 panel c) we vary the strength of feedback, as expressed by the specific momentum injection rate from a young stellar population $\langle \dot{P}/M_\star \rangle$. We achieve this by simply re-scaling the *surface densities* plugged into the model: according to the standard dimensional argument for the scaling of SFE with surface density Fall et al. (2010), these are equivalent. Because the SFE-f_{bound} relation (Figure 3) is robust to the specifics of feedback, this rescaling procedure should also model the consequences of varying $\langle \dot{P}/M_\star \rangle$ for f_{bound}. As expected from Equation 7, varying $\langle \dot{P}/M_\star \rangle$ for f_{bound} by a factor of 2 simply rescales the masses of stellar associations inversely. However the masses of bound clusters are *doubly* sensitive, varying by a factor of ~ 4, because the variation in f_{bound} compounds with the variation in ϵ_{int}. Cluster masses are therefore highly sensitive to the strength of stellar feedback.

The effect of varying metallicity in shown in Figure 8 panel d) is subtle: although we found that f_{bound} is systematically greater at lower metallicity (Figures 4-3), most of this extra mass shows up in the more bottom-heavy tail of the mass distribution, leaving the maximum cluster mass virtually unaffected.

Panel e) shows the sensitivity of the model to cloud-to-cloud variance in ϵ_{int} and f_{bound}, as driven by variance in Σ_{GMC} or the intrinsic variance parametrized by σ_{b}. Varying σ_{b} alone at the factor of 2 level has very subtle effects, but varying $\sigma_{\log \Sigma_{\mathrm{GMC}}}$ clearly affects both the maximum stellar association and bound cluster masses. Setting both variances to 0 reduces the maximum cluster mass by nearly an order of magnitude: the maximum cluster mass can then be never be greater than $f_{\mathrm{bound}} (\Sigma_{\mathrm{GMC}}) \, \epsilon_{\mathrm{int}} (\Sigma_{\mathrm{GMC}}) \, M_{\mathrm{GMC,max}}$, with the respective efficiency factor given by Equations 7 and 8 amounting to $\sim 10^{-3}$, much less than the typical factor of $\sim 10^{-2}$ separating the largest cluster mass in a given galaxy from the largest GMC mass.

Finally, in Figure 8 panel f) we vary the SFR assumed in the model. This is equivalent to sampling more GMCs and their resulting associations and bound clusters. The GMC mass distribution's upper cutoff becomes very apparent at higher SFR, while it becomes difficult to constraint for lower SFR. Because sampling more clouds samples makes rare, highly-efficient events more likely to occur in a given time window, the maximum masses of stellar associations and clusters in a given age window both scale with the SFR. The run with SFR is approximately $\propto \mathrm{SFR}^{\frac{1}{2}}$, similar to the observed relation between the brightest cluster mass and the galactic SFR (Bastian 2008).

5 COMPARISON WITH OBSERVATIONS

We will now test the model described in the previous section by synthesizing mock star cluster catalogues in M83 from the prop-
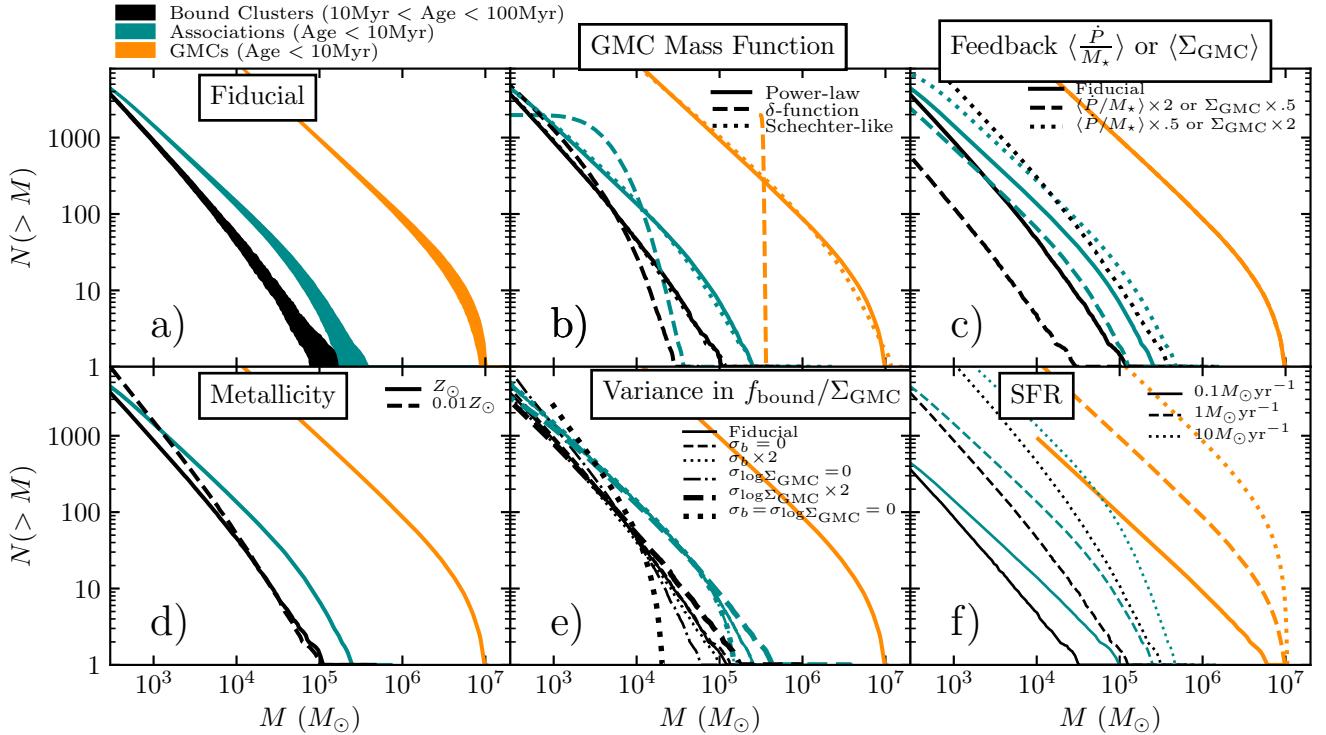
Figure 8. Results of Monte Carlo sampling experiments of our cluster formation model (§4) in a one-zone galaxy model with a continuously-forming GMC population of a certain size and mass distribution. We map the properties of GMCs (orange) onto the cumulative mass functions of young stellar associations (blue) and bound clusters (black), showing distributions in 10Myr age windows for GMCs and associations, and 90Myr windows for bound clusters, corresponding to typical age ranges considered in observations. Contours show $\pm\sigma$ intervals over 100 time windows, curves show median values. **a)** Fiducial model: a $\propto M^{-2}$ power-law GMC mass distribution truncated at 10^4 and $10^7 M_\odot$, with $\langle\Sigma_{\rm GMC}\rangle = 50 M_\odot \, {\rm pc}^{-2}$, $\sigma_{\log\Sigma_{\rm GMC}} = 0.3$dex, sampled at a rate so that the galactic SFR is $1 M_\odot \, {\rm yr}^{-1}$. Contours show $\pm\sigma$ intervals over 100 realizations. **b)** Varying the GMC mass distribution, for the fiducial power-law, Schecter-like, and Dirac δ-function forms. **c)** Varying the strength of stellar feedback $\langle\dot{P}/M_\star\rangle$, roughly equivalent to inversely varying $\langle\Sigma_{\rm GMC}\rangle$. **d)** Varying metallicity. **e)** Varying σ_b and $\sigma_{\log\Sigma_{\rm GMC}}$, which affect the intrinsic variance in $f_{\rm bound}$ and $\epsilon_{\rm int}$. **f)** Varying the galactic SFR.

erties of its GMCs. We use the Freeman et al. (2017) catalogue, taking $M_{\rm GMC}$ to be the mass inferred from the clouds' CO luminosity, and correcting the effective radii by a factor of $\sqrt{\frac{15}{2\pi}}$ to obtain $R_{\rm GMC}$, as defined in Equation 14. We assume a radially-dependent metallicty, with a central metallicity of +0.2dex with a metallicity gradient of -0.04dex pc^{-1} (Hernandez et al. 2019). We bin the GMCs and clusters by galactocentric radius as in Adamo et al. (2015), with bin edges 0.45, 2.3, 3.2, 3.9, and 4.5 kpc. The galactic SFR is $1.2 M_\odot$, and we use the respective binned SFRs given in Adamo et al. (2015).

5.1 Sampling procedure

To synthesize cluster populations, we simply repeat the Monte Carlo procedure in Section 4.3 using the observed properties of the GMCs instead of sampling from an assumed distribution in the mass-size plane. We are equipped with the observed distribution of *currently present* and *observable* GMCs, so to obtain $\frac{{\rm d}N_{\rm GMC}}{{\rm d}t \, {\rm d}M_{\rm GMC}}$ we must apply some re-sampling procedure to account for cloud lifetimes and for incompleteness. For incompleteness, we weight the sampling probabilities of each cloud inversely to the mass-dependent completeness fraction given in Freeman et al. (2017). To account for cloud lifetimes, we consider two possible simple as-

sumptions. Applying no additional re-weighting models a constant cloud lifetime, which gives $\frac{{\rm d}N_{\rm GMC}}{{\rm d}t \, {\rm d}M_{\rm GMC}}$ the same shape as the observed present mass distribution. Scaling the respective sampling weights $\propto t_{\rm ff}^{-1} = \frac{\pi}{2}\sqrt{\frac{R_{\rm GMC}^3}{G M_{\rm GMC}}}$ models the case where the cloud lifetime is $\propto t_{\rm ff}$. Present observations can hardly differentiate the two pictures (within a given galaxy), and the latter assumption has physical motivation, so we adopt the latter as our preferred model. However we still present basic results for both cases in Figures 10 and 9, and find that this ambiguity hardly affects our results in practice.

5.2 Caveats and approximations

Our procedure for inferring $\frac{{\rm d}N_{\rm GMC}}{{\rm d}t \, {\rm d}M_{\rm GMC}}$ from the data and comparing the projected cluster population with observations has two major caveats. We predict cluster formation in presently-observed GMCs but compare these clusters with a catalogue of clusters formed as much as 100Myr ago, so we expect agreement only if the SFR and ISM conditions in the respective radial of M83 have remained steady over at least that time-scale, which is not guaranteed. The comparison also requires that the dynamical evolution and disruption of the clusters has been negligible over this time-scale, ie. the observed masses and sizes have not deviated significantly from
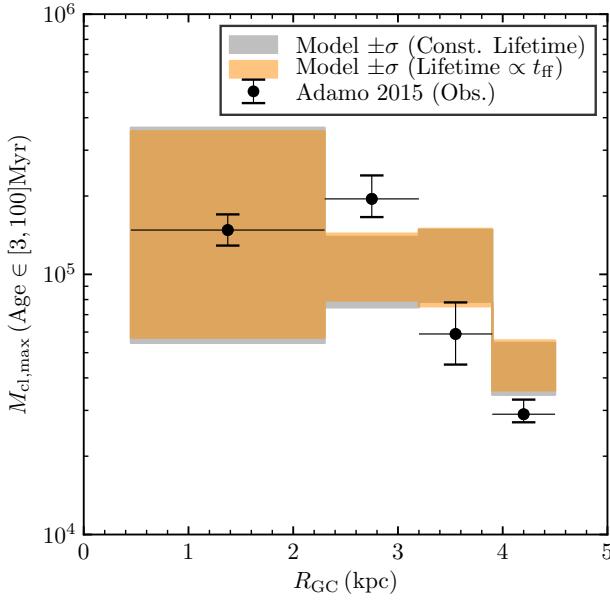
Figure 9. Comparison of the maximum bound star cluster mass from our Monte Carlo simulation of M83's cluster population with data from the Adamo et al. (2015) star cluster catalogue, in four different radial bins and 97Myr age windows (see §5 for details). Shaded regions show the $\pm\sigma$ intervals over all observation times, assuming either constant GMC lifetimes (grey) or $\propto t_{\rm ff}$ lifetimes (orange) (§5.1).
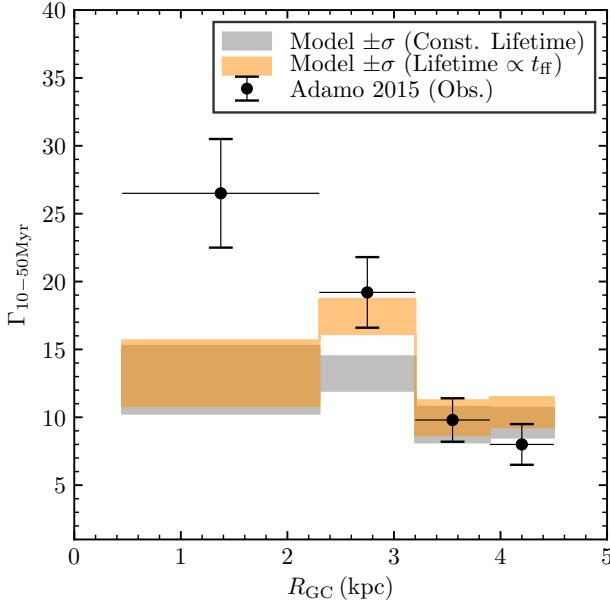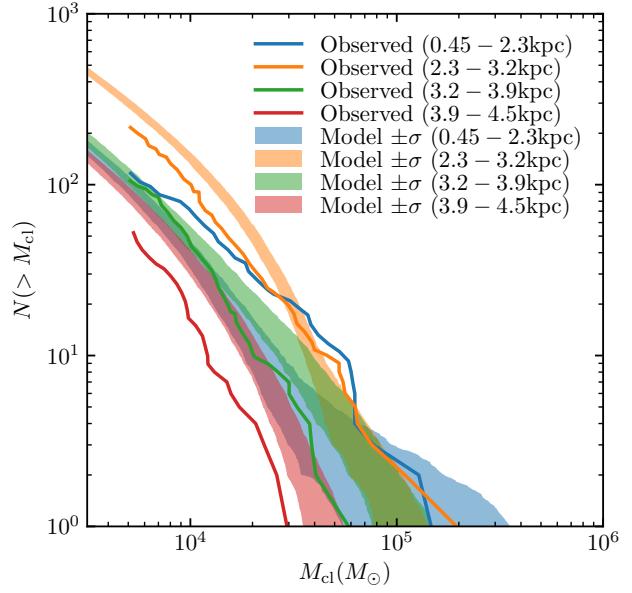

Figure 11. Predicted cumulative distributions of cluster masses of our Monte Carlo simulation of the M83 cluster population, compared with Adamo et al. (2015) in 4 radial bins and 97Myr windows, assuming GMC lifetimes scale $\propto t_{\rm ff}$. Shaded regions show the $\pm\sigma$ contours over all observation times of the model.

Figure 10. Comparison the predicted bound cluster formation efficiency $\Gamma_{10-50{\rm Myr}}$ in our Monte Carlo simulation of M83's cluster population with data from the Adamo et al. (2015) star cluster catalogue, in four different radial bins and 40Myr age windows (see §5 for details). Shaded regions show the $\pm\sigma$ intervals over observation times, assuming either constant GMC lifetimes (grey) or $\propto t_{\rm ff}$ lifetimes (orange) (§5.1).

Figure 12. Predicted galactic size-mass relation of clusters in our Monte Carlo simulation of the M83 star cluster population, compared with data from (Ryon et al. 2015) for clusters in the age range 10−300Myr. The curve indicates the median value over all observation times, and the shaded region indicates the $\pm\sigma$ quantiles. Bars on data points indicate $\pm\sigma$ uncertainties.

their masses and sizes at formation, which are the quantities predicted by the model. Stellar mass loss alone implies that this is not strictly true for any cluster: a bound cluster in isolation will decrease in mass and increase in radius over time. The effects of internal dynamical relaxation and the galactic tidal field upon the cluster will further compound mass loss and and radius increase. However, we neglect these processes here under the assumption that their effects on observables are small over the $\sim 100\,$Myr time-scales we consider.

5.3   Results

First, we predict the maximum cluster mass expected to form in each region of the galaxy, observing the maximum cluster mass present in each 97 Myr window in the Monte Carlo simulation of each radial bin. In Figure 9 we compare the $\pm\sigma$ intervals of the Monte Carlo results with the Adamo et al. (2015) catalogue, for the two different assumptions about cloud lifetimes outlined in 5.1. We find that the most massive cluster observed in a 97 Myr age window can vary considerably over time, by $\sim 0.5\,$dex in the 3 outermost bins and by nearly 1 dex in the innermost bin. In all cases our results are within 2σ of observed masses, with no systematic residual trend, so our predicted maximum cluster mass is in reasonably good agreement with observations. The assumption about cloud lifetimes hardly affects this statistic at all, because the few most extreme clouds that produce the most extreme clusters are generally getting sampled regardless of the sampling scheme.

Next, in Figure 10 we plot the mass fraction of star formation in bound clusters in 40 Myr windows, $\Gamma_{10-50\mathrm{Myr}}$, to compare with values measured in Adamo et al. (2015). $\Gamma_{10-50\mathrm{Myr}}$ also has intrinsic variation from window to window of $0.2 - 0.3\,$dex. This variation is much greater than the intrinsic variation of the SFR within the Monte Carlo model – rather, it is driven by the varying respective f_{bound} of the GMCs sampled. In a realistic scenario where the SFR *is* varying intrinsically on kpc scales by an appreciable amount, this variation in $\Gamma_{10-50\mathrm{Myr}}$ would be even greater. Hence the amount of variation we predict is really a lower bound. With the exception of the innermost bin, the model predictions are 1σ-compatible with observations with no systematic residual trend, so the model is mostly in very good agreement with observations.

The largest discrepancy is in the innermost $(0.5 - 2.3\,$kpc$)$ bin, in which we underestimate Γ by a factor of ~ 2: to match observations, our model would require greater values Σ_{GMC} to increase f_{bound} at the cloud level, and while there is a weak gradient in Σ_{GMC} in M83, it is very weak outside of the galactic center $< 0.5\,$kpc. Note that our innermost bin has a galactic dynamical time at most $t_{\mathrm{dyn}}(2.3\,$kpc$) \sim \Omega(2.3\,$kpc$)^{-1} \sim 15\,$Myr (Lundgren et al. 2004), shorter than the 40 Myr age range of the observed cluster sample. As such, in this instance it is quite possible that presently-observed GMCs are not representative of those GMCs that formed the presently-observed clusters, as the region has experienced roughly an orbit's worth of evolution.

In Figure 11 we plot the mass distributions in 97 Myr windows to compare with those plotted in Adamo et al. (2015), under the assumption that the GMC lifetime scales $\propto t_{\mathrm{ff}}$. In all radial bins the mass functions are generally within 1σ agreement with observations, modulo the uncertainties detailed in §5.1. Since we have neglected mass loss and disruption, our results are consistent with a picture where these effects upon the cluster mass function are small over $\sim 100\,$Myr time-scales in M83.

Finally, we plot the modeled size-mass relation for clusters in the $10 - 300\,$Myr age bin in Figure 12, comparing with the data provided by Ryon et al. (2015). Although our cloud-level size-mass relation gives $r_{\mathrm{h}} \propto M_{\mathrm{cl}}^{1/3}$ for a given set of cloud properties, the result of convolving the model over the GMC size-mass distribution is slightly flatter, with slope $\sim 1/4$, which is consistent with the slopes fitted in Ryon et al. (2015). We find an intrinsic scatter in the size-mass relation of $\sim 0.4\,$dex, which is mainly driven by the intrinsic scatter arising from the star formation process in our model (§3.6). Although we have neglected the effects of cluster evolution, we anticipate two main effects. First, the cluster sizes will become systematically larger with age due to mass loss and dynamical relaxation, so the normalization of the relation will increase. Second, clusters that initially formed too puffy will be subject to disruption in the galactic environment, while clusters that initially formed too compact will undergo dynamical evolution over shorter time-scales, causing them to puff up (Kruijssen et al. 2011). The net result will be a gradual reduction in the scatter of the size-mass relation.

6   DISCUSSION

Having developed and validated a model for the formation of stellar associations and bound star clusters from GMCs, we now discuss various implications of the model, the interpretation of various phenomena within this framework, and compare the framework with other works.

6.1   The importance of stellar feedback in cluster formation

According to our simulations, stellar feedback that can moderate star formation in GMCs appreciably is an essential ingredient in any model attempting to explain the masses of young, massive star clusters in the local Universe. Without feedback, our model would convert $> 50\%$ of GMC mass into star cluster mass, resulting in star cluster masses far in excess of what is observed.

Our model does assume that the GMCs in question are gravitationally bound, and in principle an alternative model to feedback-moderated star formation in GMCs is that GMCs are not gravitationally bound. However, the majority of observed massive $(> 10^6 M_\odot)$ GMCs do have virial parameters that are consistent with gravitational boundedness (Bolatto et al. 2008; Kauffmann et al. 2013; Heyer & Dame 2015; Rice et al. 2016; Miville-Deschenes et al. 2017). In particular, the clouds in the Freeman et al. (2017) catalogue we have focused on in this work tend to have virial parameters consistent with boundedness, so a lack of boundedness cannot explain their low SFEs.

6.2   The importance of stochasticity in f_{bound}

We have shown that star formation efficiency is not a one-to-one predictor of f_{bound} (Figure 3). Moreover we find that there is no cloud bulk property that predicts f_{bound} better than Σ_{gas}, which does so rather loosely, motivating our statistical approach. This suggests that the bulk properties of a GMC do not contain sufficient information to predict the detailed properties of its star clusters in a deterministic sense.

This is intuitive if one considers the large dynamic range separating the scale of clusters $(\sim 1\,$pc$)$ and clouds. The SFE will depend upon the balance of feedback and gravity on the scale of the cloud, and thus has relatively little scatter (Figure 2). Meanwhile, f_{bound} depends on the details of the small-scale cluster-forming gas flow, which can be decoupled from the cloud-scale properties.

6.3 The initial mass function of star clusters

6.3.1 Slope

The mass distribution of star clusters is the most fundamental statistic of a star cluster population. It has been measured in various local galaxies, with the typical finding that it is well-fit by a power-law of the form

$$\frac{dN_{cl}}{dM_{cl}} \propto M_{cl}^{\alpha_M}, \tag{21}$$

with α_M being typically ~ -2, with some, but relatively little variation when measured across entire galaxies (Chandar et al. 2015; Krumholz et al. 2019; Adamo et al. 2020). The simplest explanation for this mass function is that GMCs also have a mass function of this form. Although GMC mass functions are typically measured to be top-heavy (ie. slope shallower than -2), it can be argued that the GMC lifetime is likely mass-dependent ($t_{ff} \propto M^{\frac{1}{4}}$ at fixed Σ_{GMC}), and thus the distribution of *cloud formation rates*, which longer-lived clusters should trace, is steeper (Fall et al. 2010), and hence the cluster mass function is inherited from the GMC mass function, assuming a constant SFE and no cloud-to-cluster multiplicity.

Our Monte Carlo experiments with a power-law GMC mass function in §4.3 show that this logic does hold approximately for the mapping from the GMC mass function to *stellar associations*, as the stellar association mass function is roughly the GMC mass function convolved with a log-normal peaked at the typical GMC star formation efficiency, which is mass-independent at fixed Σ_{GMC} within our model.

However, we find in §4.3 that the mass function of bound star clusters generally comes out somewhat steeper than -2 (~ -2.4). While some galaxies do have steeper mass function slopes (e.g. M83, §5), -2 *does* appear to be the typical value obtained in galactic-scale mass function fits (Krumholz et al. 2019). Mass-dependent disruption or mass loss would tend to flatten the mass function if it disproportionately affects low-mass clusters, which is the general result for *all* proposed evolutionary processes except for dynamical friction (which affects more massive clusters). There is evidence for such such age-dependent flattening in M83 and M51 (Bastian et al. 2012; Messa et al. 2018). Meanwhile, in M31, where the age function implies negligible disruption over ~ 100Myr time-scales (Johnson et al. 2017), the mass function is steep (~ -2.5).

In general, our model suggests that the slope of star cluster mass functions is only universal insofar as GMC mass functions and star cluster mass loss and disruption are universal, and can change as a function of cluster age.

6.3.2 High-mass cut-off

In certain instances where it has been possible to get good statistics on star clusters within a certain localized region of a galaxy (Adamo et al. 2015; Johnson et al. 2017), some evidence has been found for a "Schechter-like" truncation in the mass function, ie.

$$\frac{dN_{cl}}{dM_{cl}} \propto M_{cl}^{\alpha_M} \exp\left(\frac{-M_{cl}}{M^\star}\right), \tag{22}$$

This may reflect some important characteristic physical scale encoded in the structure of the ISM, in star formation physics, or in galactic dynamics. According to our model, a bound fraction of ~ 1 is theoretically possible for any cloud, and so the absolute maximum bound cluster mass that can form is simply

$$M_{cl,max} = \epsilon_{int,max} M_{GMC,max}, \tag{23}$$

where the maximum integrated SFE $\epsilon_{int,max}$ depends upon the maximum Σ_{GMC} as given by Equation 7. Thus, interpreted in this manner, a truncation in the cluster mass function is the result of a truncation in the GMC mass function (Kruijssen 2014). It has been proposed that this truncation is set by the Toomre mass, the maximum mass that can collapse against galactic shear (and possibly feedback) (e.g. Hopkins 2012; Reina-Campos & Kruijssen 2017), and this picture agrees well with observations in M83 (Freeman et al. 2017).

6.3.3 Low-mass cut-off or shallowing

Some low-mass cutoff or shallowing in the mass function of bound clusters must exist, if observed galactic mass functions with slopes ≤ -2 in the observed range are to contain finite overall mass. This is difficult to constrain directly in nearby galaxies, as it requires knowledge of two uncertain incompleteness corrections: observationally, catalogues are typically incomplete in the mass range below a few $10^3 M_\odot$ (Adamo et al. 2017), and physically, low-mass clusters are also those most subject to disruption and mass loss in the galactic environment. Despite these difficulties, the low-mass regime is an important ingredient for modeling star cluster populations (e.g. Pfeffer et al. 2018), and may well depend sensitively upon star formation and feedback physics (Trujillo-Gomez et al. 2019).

We find no evidence of a lower cut-off in the star cluster mass function in any of our models that is not simply consistent with simulation resolution – the mass function exhibits power-law behaviour as far down as can be resolved (Figures 5, 6). Therefore, either no low-mass cutoff or shallowing exists in our solution, or if it does, it is at a mass that is insufficiently resolved. As such, our results concerning the low-mass cluster initial mass function are inconclusive. But even with infinite mass resolution, addressing this question properly in numerical simulations will require some treatment of the granularity of stars, for both realistic stellar feedback and stellar dynamics. The IMF sampling effect proposed in Trujillo-Gomez et al. (2019) is not captured by a feedback treatment adopting IMF-averaged feedback rates, and either requires some sampling scheme (e.g. Sormani et al. 2017; Su et al. 2018), or individually-resolved stars. And the approximation of collisionless stellar dynamics is inapplicable when the dynamical time is comparable to the relaxation time (stellar mass scales $< 100 M_\odot$), so collisional stellar dynamics could potentially affect the assembly process of low-mass clusters.

6.4 Globular cluster formation

A long-standing problem in star cluster formation is why star clusters in excess of $10^6 M_\odot$ formed in the early history of the Milky Way, now present as globular clusters (Harris 1996), but the mass scale of the most massive young star clusters in the present-day Milky Way is two orders of magnitude less (Portegies Zwart et al. 2010).

There are two possible pictures for the behaviour of the galactic cluster IMF that might explain this. First, observed young star cluster mass functions often have a $\propto M^{-2}$ form with no well-constrained truncation mass (e.g. Chandar et al. 2017; Mok et al. 2019; Adamo et al. 2020). Therefore, assuming that star cluster formation can be understood as a galaxy-wide statistical process in which this mass function is being sampled, one would expect to sample only a few very massive clusters throughout the galactic

history. Thus it is not necessarily required for the underlying distribution to change over cosmic time. In §4.3 we found that while holding our mass function fixed, simply varying the SFR was sufficient to drive variations in the maximum observed mass at a given time in accordance with the observed relation with galactic SFR (Bastian 2008), so sampling effects *are* clearly important to consider when deriving inferences about the e.g. the maximum star cluster mass.

The other possibility is that the initial cluster mass function observed over a certain of time in the galaxy does have a physical truncation imposed by the ISM conditions, as discussed in 6.3, and is not well-described by a pure power-law. This is found in M31 (Johnson et al. 2017) and possibly in M51 (Messa et al. 2018; Mok et al. 2019). To produce the most massive clusters, this truncation mass would then have to vary over the history of the galaxy, from large values at early times to smaller values today. According to our model, this picture is likely to be a better description of the galactic cluster formation history based on what is known about how galactic ISM conditions did indeed vary over time. Specifically, high-redshift galaxies had larger gas fractions (allowing more massive GMCs to form) (Tacconi et al. 2020) and higher mid-plane ISM pressures (Faucher-Giguère et al. 2013; Gurvich et al. 2020), leading to higher GMC surface densities and SFEs.

Within this second picture, an important detail to be clarified is the role of galactic mergers in generating the conditions that are favourable for GC formation. This should ultimately imprint upon the age-mass-metallicity statistics of the GC population. In cosmological simulations that trace the formation and evolution of GCs with a sub-grid model (E-MOSAICS), Kruijssen et al. (2019a) found that mergers are subdominant for GC formation. However, in simulations that resolved *individual* cluster formation with a *resolved* ISM, (Li et al. 2019) found that mergers greatly enhance the efficiency of cluster formation and thus play an important role. Kim et al. (2018a) and Ma et al. (2020) simulated the formation of *dynamically-resolved* globular clusters, and both found that mergers do play a special role in generating the conditions necessary to form the most massive GC candidates. In these works, the high-pressure conditions present during mergers appear to allow the formation of self-gravitating gas clouds with high surface density, which in turn leads to high ϵ_{int} and f_{bound}. However, those simulations could not be run to redshift 0, so it is not clear how these clusters relate to the population of GCs that are presently observed. They instead focus upon $z > 5$, ie. before the $z \sim 2$ peak of GC formation predicted by E-MOSAICS (Reina-Campos et al. 2019), so results pertaining to the importance of mergers may not generalize to GC formation as a whole.

6.5   Comparison with Kruijssen 2012

In Adamo et al. (2015), it was found that the Kruijssen (2012) (hereafter K12) model was able to predict the observed f_{bound} with an accuracy that is comparable to the present work (Fig 10). It was then combined with the Kruijssen (2014) formula to predict the maximum star cluster mass (here using our notation):

$$M_{cl,max} = \epsilon_{int} f_{bound} M_{Toomre}, \tag{24}$$

where M_{Toomre} is the maximum gas mass that can collapse according to the Toomre instability, and ϵ_{int} was given an assumed fiducial value of 5%. Again, $M_{cl,max}$ was predicted with an accuracy comparable to the present work (cf. Figure 9). It is illustrative to compare and contrast this framework with the one in the present work.

K12 and this work present the same overall physical picture: hierarchical star formation produces stars over a wide range of densities, and in denser conditions feedback is less able to moderate star formation, leading to more efficient bound star cluster formation. However, the models do have important quantitative differences regarding the details of feedback-moderated star formation.

To summarize, K12 modeled the galactic ISM using the density statistics of isothermal, supersonic turbulence (Krumholz & McKee 2005), which are fixed by three galactic bulk parameters: the Toomre stability parameter Q, the mean disk gas surface density Σ_{gas}, and the orbital frequency Ω. These determine a log-normal gas density PDF which, according to the hierarchical star formation paradigm, maps onto the distribution of densities ρ at which stars form. A feedback time-scale t_{fb} is introduced, identified with the time required for feedback to disrupt a gas overdensity and halt star formation, on the order of several Myr, with only weak residual dependence on the three parameters (note that alternate feedback formulations can be slotted into the model, and this is merely the fiducial model). Locally-high ϵ_{int} occurs in the upper tail of the gas density distribution where $t_{ff} \ll t_{fb}$, as star formation can proceed with a per-freefall efficiency of $\sim 1\%$ for many freefall times until $\epsilon_{int} \sim 1$ locally, and the bound fraction can be correspondingly high.

This picture starts with the same premises (ISM physics and stellar feedback) and arrives at the same conclusion (locally-high SFE and bound cluster formation in dense regions) as the present work, but some differences should be noted between what is assumed in the analytic calculations, and what is found our simulations, and other recent, qualitatively-similar simulations (Geen et al. 2017; Kim et al. 2018b; Li et al. 2019). We find that the per-freefall SFE is not universal (Grudić et al. 2018a), nor in any detailed agreement with turbulence-regulated derivations of ϵ_{ff} such as Krumholz & McKee (2005), the different assumptions considered in K12. Simulations of feedback-moderated star formation on GMC scales typically find that ϵ_{ff} and ϵ_{int} are intimately linked to one another (consistent with recent observations, see Kruijssen et al. 2019b; Chevance et al. 2020b), and scale with cloud parameters in a manner similar to Equation 7. Hence the value $\epsilon_{ff} \sim 1\%$ is expected to be emergent, and to depend sensitively upon stellar feedback physics. The dimensional scalings of the *fiducial* feedback model in K12 and the present work also differ. The quantity t_{fb} is a characteristic *time-scale* that determines SFE and f_{bound}, while the characteristic quantities Σ_{crit} and Σ_{bound} in our model predict scalings with GMC gas surface density. K12 did consider an alternate model with a similar scaling, formulating an assuming instantaneous radiative feedback without any time delay, but found that this predicted values of f_{bound} that would be difficult to distinguish from their fiducial model in observations. Therefore, while numerical simulations could potentially inform extensions or corrections to the assumptions made in K12, it is not clear that its results would be strongly affected. This suggests that the elements in common between K12 and the present work represent the key physics driving stellar cluster formation.

7   SUMMARY AND FUTURE WORK

In this work we have used numerical simulations of star-forming GMCs to explore the mapping between GMCs and the star clusters that they form. We have found that mapping is complex, and not one-to-one, due to of the variety of outcomes made possible by stochastic variations in the internal turbulent flows of the clouds.

In essence, the overall SFE of GMCs is reasonably predictable because the efficiency of feedback depends upon the *macrostate* of the cloud, whereas cluster formation occurs on much smaller scales within the cloud, and is thus determined by the specific *microstate* of the turbulent gas motions leading to star formation.

Despite this complexity, we have been able to explore the range of variations from one microstate to another and have found that the mapping from clouds to clusters does admit a statistical model (Section 4) that encodes fairly simple scalings in cluster formation efficiency, star cluster sizes, and star cluster masses. When we apply this model to a real population of GMCs, we successfully predict the fraction of star formation in bound clusters, the maximum cluster mass, and the size distribution of massive clusters. This is one of the first instances in which numerical simulations have succeed at reproducing the properties of star clusters in detail, using the observed GMC properties as initial conditions. Our key findings are as follows:

• Essentially all GMCs will form some fraction of their stars in bound clusters – the formation of bound clusters and unbound associations are part of the same continuum, and not distinct processes (e.g. Kruijssen 2012). The star formation efficiency ϵ_{int} and the bound fraction of star formation f_{bound} are correlated, but distinct quantities (Figure 3). Both scale as an increasing function of the cloud surface density Σ_{GMC}, eventually saturating to an order-unity value (eg. Fall et al. 2010; Murray et al. 2010; Grudić et al. 2018a).

• f_{bound} scales steeply with Σ_{GMC}, from a typical value of a few per cent in GMCs with surface density $\sim 50\,M_\odot\,pc^{-2}$ in our galaxy (Goddard et al. 2010), to $10-30\%$ in nearby spiral galaxies in which GMC surface densities are systematically a factor of ~ 2 higher (Faesi et al. 2018). The cloud-scale f_{bound} saturates to ~ 1 when the cloud scale SFE is $10-20\%$, in good agreement with Li et al. (2019).

• For a given set of cloud parameters, f_{bound} exhibits large variations, especially at low Σ_{GMC}. We construct a statistical model that reproduces the scatter in simulation results shown in Figure 4 (Equations 9 and 10).

• GMCs generally form multiple bound clusters, with masses distributed according to a cloud-scale mass distribution (Equation 11). The primary cluster tends to have a large (10-90%) of the the total bound mass.

• Stellar feedback is crucial in setting star cluster properties. Radiation is the most important, stellar winds are somewhat important, and SNe are essentially irrelevant because they come too late (see Table 2). Because cluster masses are so sensitive to the strength of feedback (Figure 11), they provide a tight observational constraint on it.

• The formation of bound clusters from 1% solar metallicity gas is more efficient than at solar metallicity (Figure 4). We have isolated this effect to the weaker stellar wind feedback expected from low-metallicity OB stars (Section 3.6.1), whose winds are effectively irrelevant compared to other feedback mechanisms.

• The weak size-mass relation of star clusters is set during the star formation process, which produces large intrinsic scatter in cluster radii. There is a relation, however: star clusters from a given cloud form with a 3D density that depends upon the bulk properties of the parent cloud (Equation 13). While our predicted size function is subject to some numerical caveats (§3.6), our model still gives predictions in good agreement with observed cluster sizes (§5).

Though our success in reproducing star cluster bulk properties is encouraging, the problem of star cluster formation is hardly solved. Because our method of simulating star formation is approximate, we anticipate that comparisons with observed cluster properties that go beyond simple bulk properties will reveal interesting discrepancies. The extragalactic observations that we have compared with are likely the *easiest* constraints to satisfy. Meanwhile, the detailed cluster kinematics, and temporal and spatial age distributions that can be observed in the Milky Way and its satellites may well provide more powerful constraints on the star formation process.

At this point, it is likely that the most worthwhile gains in simulation realism can only be made by attacking the harder version of the problem: resolving the formation and motion of individual stars self-consistently, rather than assuming the IMF and using a simple stellar population formalism. Our simulations are reaching the scales where the granularity of stars can easily become important, and the details of how and when individual stars form can have major implications for stellar feedback, and hence the subsequent cloud evolution (Grudić & Hopkins 2019). Due to computational cost, this has never been done on the scale of massive GMCs that can actually sample the IMF, and hence the effects of feedback from massive stars have yet to be demonstrated in a fully self-consistent calculation that *predicts* massive star formation with conclusive numerical convergence. However, the advent of massively-scalable, Lagrangian codes with fast, accurate MHD methods and well-developed feedback coupling techniques will soon make this possible: in Guszejnov et al. (2020a) we simulated GMCs up to $2 \times 10^6 M_\odot$ with individually-resolved collapsing stellar cores without feedback, at a mass resolution 200 times finer than the present work. In future work we will present results with a full accounting of both protostellar and stellar feedback (Grudić et al. 2020, in prep., Guszejnov et al. 2020, in prep.).

Questions of particular importance for the next generation of GMC simulations include the behaviour of protostellar and main-sequence feedback acting in concert (ie. does regulating star formation on small scales ultimately affect cloud-scale behaviour?), what are the necessary and sufficient physics to satisfy constraints on the IMF turnover mass (e.g. Bate 2009; Krumholz 2011; Federrath et al. 2017; Guszejnov et al. 2016, 2019), and what deviations from universality might be expected in different environments. These are questions that can only be addressed by a comprehensive, individually-resolved approach to stellar feedback and dynamics.

DATA AVAILABILITY

The data supporting the plots within this article are available on reasonable request to the corresponding author. A public version of the GIZMO code is available at http://www.tapir.caltech.edu/~phopkins/Site/GIZMO.html.

REFERENCES

Adamo A., Kruijssen J. M. D., Bastian N., Silva-Villa E., Ryon J., 2015, MNRAS, 452, 246
Adamo A., et al., 2017, ApJ, 841, 131
Adamo A., et al., 2020, Space Sci. Rev., 216, 69
Barnes J., Hut P., 1986, Nature, 324, 446
Bastian N., 2008, Monthly Notices of the Royal Astronomical Society, 390, 759
Bastian N., Gieles M., Lamers H. J. G. L. M., Scheepmaker R. A., de Grijs R., 2005, A&A, 431, 905
Bastian N., et al., 2012, MNRAS, 419, 2606
Bate M. R., 2009, MNRAS, 392, 1363
Baumgardt H., Kroupa P., 2007, MNRAS, 380, 1589
Bolatto A. D., Leroy A. K., Rosolowsky E., Walter F., Blitz L., 2008, ApJ, 686, 948
Bonnell I. A., Smith R. J., Clark P. C., Bate M. R., 2011, MNRAS, 410, 2339
Braine J., Rosolowsky E., Gratier P., Corbelli E., Schuster K. F., 2018, A&A, 612, A51
Bressert E., et al., 2010, MNRAS, 409, L54
Chandar R., Fall S. M., Whitmore B. C., 2015, ApJ, 810, 1
Chandar R., Fall S. M., Whitmore B. C., Mulia A. J., 2017, The Astrophysical Journal, 849, 128
Chevance M., et al., 2020a, Space Sci. Rev., 216, 50
Chevance M., et al., 2020b, MNRAS, 493, 2872
Choksi N., Kruijssen J. M. D., 2019, arXiv e-prints, p. arXiv:1912.05560
Colombo D., et al., 2014, ApJ, 784, 3
Dale J. E., Ercolano B., Bonnell I. A., 2015, MNRAS, 451, 987
Efremov Y. N., Elmegreen B. G., 1998, MNRAS, 299, 588
Elmegreen B. G., 1983, MNRAS, 203, 1011
Elmegreen B. G., 2002, ApJ, 577, 206
Elmegreen B. G., 2008, The Astrophysical Journal, 672, 1006
Elson R. A. W., Fall S. M., Freeman K. C., 1987, ApJ, 323, 54
Faesi C. M., Lada C. J., Forbrich J., 2018, ApJ, 857, 19
Fall S. M., Krumholz M. R., Matzner C. D., 2010, ApJ, 710, L142
Faucher-Giguère C.-A., Quataert E., Hopkins P. F., 2013, MNRAS, 433, 1970
Federrath C., Krumholz M., Hopkins P. F., 2017, in Journal of Physics Conference Series. p. 012007, doi:10.1088/1742-6596/837/1/012007
Feldmann R., Gnedin N. Y., 2011, ApJ, 727, L12
Fellhauer M., Kroupa P., 2005, ApJ, 630, 879
Fouesneau M., et al., 2014, ApJ, 786, 117
Freeman P., Rosolowsky E., Kruijssen J. M. D., Bastian N., Adamo A., 2017, MNRAS, 468, 1769
Gammie C. F., Ostriker E. C., 1996, ApJ, 466, 814
Geen S., Soler J. D., Hennebelle P., 2017, MNRAS, 471, 4844
Ginsburg A., Kruijssen J. M. D., 2018, ApJ, 864, L17
Ginsburg A., et al., 2016, A&A, 595, A27
Goddard Q. E., Bastian N., Kennicutt R. C., 2010, MNRAS, 405, 857
Gouliermis D. A., 2018, PASP, 130, 072001
Gouliermis D. A., et al., 2015, MNRAS, 452, 3508
Grasha K., et al., 2017, ApJ, 840, 113
Grudić M. Y., Hopkins P. F., 2019, MNRAS, 488, 2970
Grudić M. Y., Hopkins P. F., Faucher-Giguère C.-A., Quataert E., Murray N., Kereš D., 2018a, MNRAS, 475, 3511
Grudić M. Y., Guszejnov D., Hopkins P. F., Lamberts A., Boylan-Kolchin M., Murray N., Schmitz D., 2018b, MNRAS, 481, 688
Grudić M. Y., Hopkins P. F., Lee E. J., Murray N., Faucher-Giguère C.-A., Johnson L. C., 2019, MNRAS, 488, 1501
Gurvich A. B., et al., 2020, arXiv e-prints, p. arXiv:2005.12916
Guszejnov D., Krumholz M. R., Hopkins P. F., 2016, MNRAS, 458, 673
Guszejnov D., Hopkins P. F., Graus A. S., 2019, MNRAS, 485, 4852
Guszejnov D., Grudić M. Y., Hopkins P. F., Offner S. S. R., Faucher-Giguère C.-A., 2020a, MNRAS,
Guszejnov D., Grudić M. Y., Offner S. S. R., Boylan-Kolchin M., Faucher-Giguère C.-A., Wetzel A., Benincasa S. M., Loebman S., 2020b, MNRAS, 492, 488
Harris W. E., 1996, AJ, 112, 1487
Hernandez S., et al., 2019, ApJ, 872, 116
Heyer M., Dame T., 2015, Annual Review of Astronomy and Astrophysics, 53, 583
Hills J. G., 1980, ApJ, 235, 986
Hopkins P. F., 2012, MNRAS, 423, 2016
Hopkins P. F., 2015, MNRAS, 450, 53
Hopkins P. F., 2016, MNRAS, 462, 576
Hopkins P. F., Grudić M. Y., 2019, MNRAS, 483, 4187
Hopkins P. F., Raives M. J., 2016, MNRAS, 455, 51
Hopkins P. F., Quataert E., Murray N., 2012, MNRAS, 421, 3488
Hopkins P. F., Narayanan D., Murray N., 2013, MNRAS, 432, 2647
Hopkins P. F., et al., 2018a, MNRAS, 477, 1578
Hopkins P. F., et al., 2018b, MNRAS, 480, 800
Hopkins P. F., Grudić M. Y., Wetzel A., Kereš D., Faucher-Giguère C.-A., Ma X., Murray N., Butcher N., 2020, MNRAS, 491, 3702
Hunter J. D., 2007, Computing In Science & Engineering, 9, 90
Johnson L. C., et al., 2012, ApJ, 752, 95
Johnson L. C., et al., 2016, ApJ, 827, 33
Johnson L. C., et al., 2017, ApJ, 839, 78
Jones E., Oliphant T., Peterson P., et al., 2001, SciPy: Open source scientific tools for Python, http://www.scipy.org/
Kauffmann J., Pillai T., Goldsmith P. F., 2013, ApJ, 779, 185
Kharchenko N. V., Piskunov, A. E. Schilbach, E. Röser, S. Scholz, R.-D. 2013, A&A, 558, A53
Kim J.-h., et al., 2018a, MNRAS, 474, 4232
Kim J.-G., Kim W.-T., Ostriker E. C., 2018b, ApJ, 859, 68
Kirby E. N., Cohen J. G., Guhathakurta P., Cheng L., Bullock J. S., Gallazzi A., 2013, ApJ, 779, 102
Kroupa P., 2001, MNRAS, 322, 231
Kroupa P., Hurley J., Aarseth S., 2001, Monthly Notices of the Royal Astronomical Society, 321, 699
Kruijssen J. M. D., 2012, MNRAS, 426, 3008
Kruijssen J. M. D., 2014, Classical and Quantum Gravity, 31, 244006
Kruijssen J. M. D., Bastian N., 2016, MNRAS, 457, L24

Kruijssen J. M. D., Pelupessy F. I., Lamers H. J. G. L. M., Portegies Zwart S. F., Icke V., 2011, MNRAS, 414, 1339

Kruijssen J. M. D., Maschberger T., Moeckel N., Clarke C. J., Bastian N., Bonnell I. A., 2012, MNRAS, 419, 841

Kruijssen J. M. D., Pfeffer J. L., Crain R. A., Bastian N., 2019a, MNRAS, 486, 3134

Kruijssen J. M. D., et al., 2019b, Nature, 569, 519

Krumholz M. R., 2011, The Astrophysical Journal, 743, 110

Krumholz M. R., McKee C. F., 2005, ApJ, 630, 250

Krumholz M. R., Matzner C. D., McKee C. F., 2006, ApJ, 653, 361

Krumholz M. R., McKee C. F., Bland -Hawthorn J., 2019, ARA&A, 57, 227

Kuhn M. A., et al., 2014, ApJ, 787, 107

Kuhn M. A., Hillenbrand L. A., Sills A., Feigelson E. D., Getman K. V., 2019, ApJ, 870, 32

Lada C. J., Lada E. A., 1991, in Janes K., ed., Astronomical Society of the Pacific Conference Series Vol. 13, The Formation and Evolution of Star Clusters. pp 3–22

Lada C. J., Lada E. A., 2003, ARA&A, 41, 57

Lada C. J., Margulis M., Dearborn D., 1984, ApJ, 285, 141

Lee E. J., Chang P., Murray N., 2015, ApJ, 800, 49

Lee E. J., Miville-Deschenes M.-A., Murray N. W., 2016, ApJ, 833, 229

Leitherer C., et al., 1999, ApJS, 123, 3

Leroy A. K., et al., 2018, ApJ, 869, 126

Li H., Vogelsberger M., Marinacci F., Gnedin O. Y., 2019, MNRAS, 487, 364

Lundgren A. A., Wiklind T., Olofsson H., Rydbeck G., 2004, A&A, 413, 505

Ma X., et al., 2020, MNRAS, 493, 4315

Mathieu R. D., 1983, ApJ, 267, L97

McCrady N., Graham J. R., 2007, ApJ, 663, 844

McKee C. F., Ostriker E. C., 2007, ARA&A, 45, 565

Messa M., et al., 2018, MNRAS, 477, 1683

Miville-Deschenes M.-A., Murray N., Lee E. J., 2017, ApJ, 834, 57

Mok A., Chandar R., Fall S. M., 2019, ApJ, 872, 93

Murray N., 2011, ApJ, 729, 133

Murray N., Chang P., 2015, ApJ, 804, 44

Murray N., Quataert E., Thompson T. A., 2010, ApJ, 709, 191

Myers P. C., Dame T. M., Thaddeus P., Cohen R. S., Silverberg R. F., Dwek E., Hauser M. G., 1986, ApJ, 301, 398

Pérez F., Granger B. E., 2007, Computing in Science and Engineering, 9, 21

Pfeffer J., Kruijssen J. M. D., Crain R. A., Bastian N., 2018, MNRAS, 475, 4309

Portegies Zwart S. F., McMillan S. L. W., Gieles M., 2010, ARA&A, 48, 431

Reina-Campos M., Kruijssen J. M. D., 2017, MNRAS, 469, 1282

Reina-Campos M., Kruijssen J. M. D., Pfeffer J. L., Bastian N., Crain R. A., 2019, MNRAS, 486, 5838

Rice T. S., Goodman A. A., Bergin E. A., Beaumont C., Dame T. M., 2016, The Astrophysical Journal, 822, 52

Rosdahl J., Teyssier R., 2015, MNRAS, 449, 4380

Ryon J. E., et al., 2015, MNRAS, 452, 525

Ryon J. E., et al., 2017, ApJ, 841, 92

Schechter P., 1976, ApJ, 203, 297

Smith R., Slater R., Fellhauer M., Goodwin S., Assmann P., 2011, MNRAS, 416, 383

Smith R., Goodwin S., Fellhauer M., Assmann P., 2013, MNRAS, 428, 1303

Sormani M. C., Treß R. G., Klessen R. S., Glover S. C. O., 2017, MNRAS, 466, 407

Springel V., 2005, MNRAS, 364, 1105

Springel V., White S. D. M., Tormen G., Kauffmann G., 2001, MNRAS, 328, 726

Stone J. M., Ostriker E. C., Gammie C. F., 1998, ApJ, 508, L99

Su K.-Y., et al., 2018, MNRAS, 480, 1666

Sun J., et al., 2018, ApJ, 860, 172

Tacconi L. J., Genzel R., Sternberg A., 2020, arXiv e-prints, p. arXiv:2003.06245

Trujillo-Gomez S., Reina-Campos M., Kruijssen J. M. D., 2019, MNRAS, 488, 3972

Tutukov A. V., 1978, A&A, 70, 57

Usher C., et al., 2012, MNRAS, 426, 1475

Vink J. S., de Koter A., Lamers H. J. G. L. M., 2001, A&A, 369, 574

Vutisalchavakul N., Evans II N. J., Heyer M., 2016, ApJ, 831, 73

Ward J. L., Kruijssen J. M. D., 2018, MNRAS, 475, 5659

Ward J. L., Kruijssen J. M. D., Rix H.-W., 2020, MNRAS, 495, 663

Weiß A., Neininger N., Hüttemeister S., Klein U., 2001, A&A, 365, 571

Williams J. P., McKee C. F., 1997, ApJ, 476, 166

APPENDIX A: RESOLUTION EFFECTS UPON CLUSTER MASSES AND SIZES

In Grudić et al. (2018a) we showed that our simulation setup predicts GMC-scale SFEs that are insensitive to the effects of numerical resolution (as well as many other details that are secondary to feedback, such as star formation prescription, cooling details, and magnetic fields). However, the predictions of this work regarding masses and sizes of bound clusters must also be examined for numerical effects.

In Figure A1 we plot the cluster mass functions stacked over our 10 statistical relizations of initial turbulence for our fiducial cloud model ($M_{\mathrm{GMC}} = 4 \times 10^6 M_\odot$, $R_{\mathrm{GMC}} = 100$pc), at two different mass resolutions: 64^3 Lagrangian gas cells, and 100^3 cells (our fiducial resolution). We find that the mass functions agree well over their common resolved range, and the main difference is that the finer-resolved simulations extend to smaller masses. Hence our results for star cluster masses and f_{bound} are fairly insensitive to mass resolution except in the case where the cluster mass in question simply cannot be resolved at all.

In Figure A2 we plot the size-mass relations for these same simulations at two different resolution levels, and find that clusters formed in finer-resolved simulations are preferentially more compact. Therefore, we cannot rule out that our cluster sizes are sensitive to numerical resolution, and hence that the cluster size predictions are not fully self-consistent. Indeed, it is not clear whether it is even *possible* to self-consistently predict star cluster sizes using the collisionless approximation that we have adopted. A collisionless self-gravitating fluid conserves its maximum phase-space density (Grudić et al. 2018b), and this approximation breaks down at the scale where the collisionless approximation does, ie. in clusters where the relaxation time is comparable to the dynamical time. Therefore, we acknowledge that fully self-consistent predictions of star cluster sizes may well require a full N-body technique.

This paper has been typeset from a TeX/LaTeX file prepared by the author.
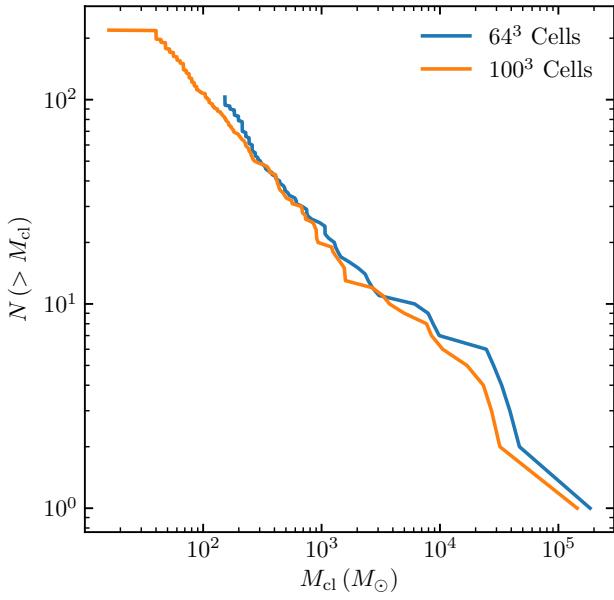
Figure A1. Cumulative mass distribution of the clusters formed in the 10 realizations of our GMC model with $M_{\rm GMC} = 4 \times 10^6 M_\odot$, $R_{\rm GMC} = 100$pc, for two different mass resolutions: 100^3 (ie. $\Delta m = 4 M_\odot$), and 64^3 (ie. $\Delta m = 15.2 M_\odot$).
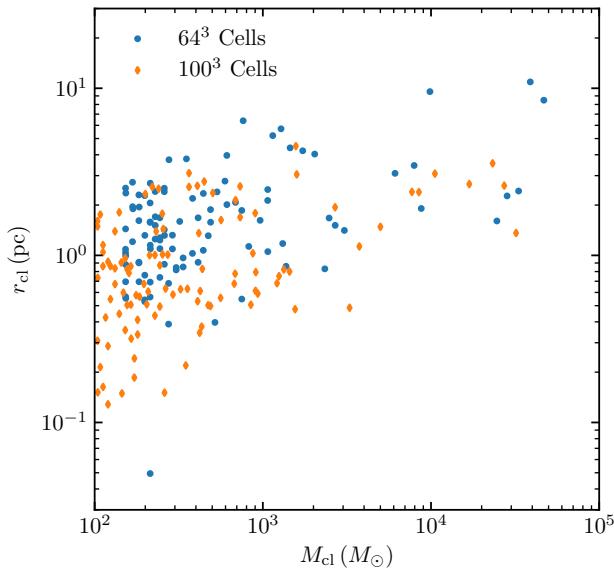

Figure A2. Size-mass relation of the clusters formed in the 10 realizations of our GMC model with $M_{\rm GMC} = 4 \times 10^6 M_\odot$, $R_{\rm GMC} = 100$pc for two different mass resolutions. Our numerical technique produces preferentially smaller clusters at higher resolution, possibly hinting at missing physics (see discussion in A).